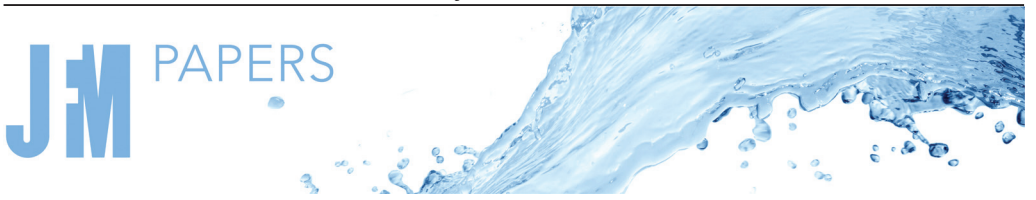
J. Fluid Mech. (2021), *vol*. 927, A28, doi:10.1017/jfm.2021.780



Competing flow and collision effects in a monodispersed liquid–solid fluidized bed at a moderate Archimedes number

Yinuo Yao[1,2,†], **Craig S. Criddle**[2] **and Oliver B. Fringer**[1]

[1]The Bob and Norma Street Environmental Fluid Mechanics Laboratory, Department of Civil and Environmental Engineering, Stanford University, Stanford, CA 94305, USA

[2]Codiga Resource Recovery Center at Stanford, Department of Civil and Environmental Engineering, Stanford University, Stanford, CA 94305, USA

(Received 20 April 2021; revised 19 August 2021; accepted 31 August 2021)

We study the effects of fluid–particle and particle–particle interactions in a three-dimensional monodispersed reactor with unstable fluidization. Simulations were conducted using the immersed boundary method for particle Reynolds numbers of 20–70 with an Archimedes number of 23 600. Two different flow regimes were identified as a function of the particle Reynolds number. For low particle Reynolds numbers ($20 < Re_p < 40$), the porosity is relatively low and the particle dynamics are dominated by interparticle collisions that produce anisotropic particle velocity fluctuations. The relative importance of hydrodynamic effects increases with increasing particle Reynolds number, leading to a minimized anisotropy in the particle velocity fluctuations at an intermediate particle Reynolds number. For high particle Reynolds numbers ($Re_p > 40$), the particle dynamics are dominated by hydrodynamic effects, leading to decreasing and more anisotropic particle velocity fluctuations. A sharp increase in the anisotropy occurs when the particle Reynolds number increases from 40 to 50, corresponding to a transition from a regime in which collision and hydrodynamic effects are equally important (regime 1) to a hydrodynamic-dominated regime (regime 2). The results imply an optimum particle Reynolds number of roughly 40 for the investigated Archimedes number of 23 600 at which mixing in the reactor is expected to peak, which is consistent with reactor studies showing peak performance at a similar particle Reynolds number and with a similar Archimedes number. Results also show that maximum effective collisions are attained at intermediate particle Reynolds number. Future work is required to relate optimum particle Reynolds number to Archimedes number.

Key words: fluidized beds, particle/fluid flow

† Email address for correspondence: yaoyinuo@stanford.edu

© The Author(s), 2021. Published by Cambridge University Press

https://doi.org/10.1017/jfm.2021.780 Published online by Cambridge University Press

1. Introduction

Fluidization has been widely found in many industrial processes such as water and wastewater treatment and chemical synthesis. In these processes, one of the key operating parameters is the flow rate, which in turn controls the porosity to achieve efficient mixing and mass transfer. Depending on the processes, the optimal operating parameter can vary significantly. By gaining a detailed understanding of the particle dynamics in the fluidized bed, system optimization would be possible. Using wastewater treatment as an illustrative example, the staged anaerobic fluidized-bed membrane bioreactor (known as SAF-MBR) was recently proposed to reduce energy demand (Shin *et al.* 2011; Shin, Bae & McCarty 2012; Shin *et al.* 2014) in which granular activated carbon (known as GAC) particles are fluidized to both maximize biological degradation rate through maximizing the growth of biofilm and minimize membrane fouling through particle collisions. Both objectives can be optimized by choosing the optimal flow rate which in turn controls the porosity. In addition to operation, elucidating the particle dynamics in a fluidized bed can provide information to model biofilm detachment rates. Important biofilm detachment mechanisms include shear stress from fluid–particle interactions and abrasion from particle–particle interactions (Nicolella, Di Felice & Rovatti 1996; Nicolella *et al.* 1997; Rittmann & McCarty 2018). However, the proposed models either fail to decouple the effect of shear stress from abrasion or only consider abrasion effects (Chang *et al.* 1991; Gjaltema *et al.* 1997; Nicolella *et al.* 1997). Without a thorough understanding of the particle dynamics, especially the competition between abrasion and hydrodynamic effects in the fluidized bed, optimizing operating parameters for efficient mixing and modelling biofilm detachment remains an elusive problem.

In the past few decades, many researchers have studied the hydrodynamics of fluidized-bed reactors (Zenit, Hunt & Brennen 1997; Di Felice 1999; Duru *et al.* 2002; Derksen & Sundaresan 2007; Verma *et al.* 2014, 2015; Yang *et al.* 2017; Lu, Peters & Kuipers 2020; Shajahan & Breugem 2020). In general, fluidized beds are classified into two different categories as either aggregative or particulate (Geldart 1973). The behaviour of fluidized beds can be further classified based on the Froude number $Fr_m = u_{mf}^2/(gd_p)$, where u_{mf} is the minimum fluidization velocity, g is the gravitational acceleration and d_p is the particle diameter (Sundaresan 2003). For $Fr_m \sim O(10^{-3})$, no bubbles are observed. For $Fr_m \sim O(10^{-2})$, bubbles appear intermittently. For $Fr_m \sim O(10^{-1})$, bubble-like voids persist. In wastewater treatment, $Fr_m \sim O(10^{-3})$ is generally assumed based on the particles used (Shin *et al.* 2014). Zenit *et al.* (1997) measured the particle pressure (collision stress) for particles with different properties over a range of volume fractions and showed that the particle pressure initially increases with decreasing volume fraction when the volume fraction is large and then decreases with further decreasing volume fraction, an effect that was also demonstrated by Derksen & Sundaresan (2007). Since particle pressure measures the effect of collisions, it can be used to quantify abrasion that leads to biofilm detachment. Although they did not directly quantify hydrodynamic stresses, Derksen & Sundaresan (2007) attempted to evaluate the importance of particle streaming stress which is a measure of the hydrodynamic pressure induced by particle velocity fluctuations. Yao, Criddle & Fringer (2021*b*) studied the effect of Archimedes number in concentrated suspensions and discovered that low Archimedes number suspensions result in long-lived particle clusters while high Archimedes number suspensions mainly consist of short-lived particle clusters.

To elucidate the effect of porosity on particle dynamics in the anaerobic fluidized bed reactor (known as AFBR), we study the fluid–particle and particle–particle interactions

https://doi.org/10.1017/jfm.2021.780 Published online by Cambridge University Press

in a fluidized bed with the Eulerian–Lagrangian (EL) method. The EL methods solve for the dynamics of individual particles and compute the Eulerian flow–discrete particle and particle–particle interactions with different collision models (Yu & Xu 2003; Akiki, Jackson & Balachandar 2016; Costa *et al.* 2015; Biegert, Vowinckel & Meiburg 2017). The EL methods can be further classified into two subcategories: (i) volume-averaged computational fluid dynamics–discrete element methods (CFD-DEM) and (ii) particle-resolved simulations (PRS). The CFD-DEM method employs various closure laws to model the momentum transfer between the discrete particles and the fluid (Yu & Xu 2003; Pan *et al.* 2016). One advantage of CFD-DEM is its ability to simulate millions of particles, as in the study of the macroscopic behaviour of particle-laden flows leading to clustering (Akiki, Jackson & Balachandar 2017*a*; Akiki, Moore & Balachandar 2017*b*). However, there is no consensus on the most appropriate closure laws to parameterize the fluid–particle interactions (Yin & Koch 2007; Tenneti, Garg & Subramaniam 2011). Another disadvantage is that the Eulerian fields are volume averaged which precludes statistical analysis of motions related to detailed fluid–particle interactions.

Because of the need for closure laws in CFD-DEM, it cannot be used to study the detailed physics of fluid–particle and particle–particle interactions in an anaerobic fluidized bed reactor. Therefore, we employ the PRS approach which can be thought of as the limiting case of the CFD-DEM method in which the Eulerian flow is computed on a grid in which many (15–30) grid cells resolve the smallest particle diameter to simulate all of the spatiotemporal scales related to the flow–particle interactions (Lee & Balachandar 2010; Lee, Ha & Balachandar 2011; Esteghamatian *et al.* 2017). As a result, the Eulerian quantities are no longer volume-averaged over many particles, which allows for a direct quantification of particle dynamics in systems like fluidized-bed reactors. Three popular approaches used to study particle-laden flows are the PHYSALIS method (Zhang & Prosperetti 2005), the immersed boundary method (IBM) and the lattice Boltzmann (known as LB) technique with comparable accuracy (Finn & Apte 2013). Recently, the PRS approach with IBM has been widely applied to a number of different problems, including extracting drag laws from arrays of particles (Tenneti *et al.* 2011; Tang *et al.* 2015; Akiki *et al.* 2017*b*) and understanding the detailed physics of flow–particle interactions in fluidized beds and particle suspensions (Yin & Koch 2007; Kriebitzsch, van der Hoef & Kuipers 2013; Uhlmann & Doychev 2014; Zaidi, Tsuji & Tanaka 2015; Esteghamatian *et al.* 2017; Ozel *et al.* 2017; Willen & Prosperetti 2019).

In this paper, we present PRS results of a fluidized bed reactor to gain a detailed understanding of the effects of varying upflow velocity on the particle dynamics. A series of cases with different particle Reynolds numbers is studied and the simulation results are used to (1) understand the equilibrium behaviour of particle fluctuations, (2) establish links between particle velocity fluctuations, forces on particles and flow–particle microstructure and (3) identify various flow regimes and momentum transfer mechanisms as a function of the particle Reynolds number.

2. Numerical methodology

2.1. *Equations and discretizations*

The governing Navier–Stokes equations are solved in a three-dimensional flow reactor with a square cross-section and with an array of uniform spherical particles. Direct forcing by the IBM method is accounted for with a source term, $\boldsymbol{f}_{IBM}$, which is added to the Navier–Stokes equation and enforces no-slip boundary conditions on the particle surfaces.

https://doi.org/10.1017/jfm.2021.780 Published online by Cambridge University Press

With this forcing, the incompressible Navier–Stokes equation we solve is given by

$$\frac{\partial \boldsymbol{u}}{\partial t} + \boldsymbol{u} \cdot \nabla \boldsymbol{u} = -\nabla p + \nu \nabla^2 \boldsymbol{u} + \boldsymbol{f}_{IBM}, \tag{2.1}$$

subject to continuity, $\nabla \cdot \boldsymbol{u} = 0$, where $\boldsymbol{u}$ is the velocity vector and p is the pressure normalized by the fluid density, ρ_f. These equations are discretized on a uniform collocated Cartesian grid and momentum and pressure are coupled with the fractional step method (Zang, Street & Koseff 1994). The advection term is discretized with the explicit, three-step Runge–Kutta schemes described in Rai & Moin (1991). The viscous term is discretized with the implicit Crank–Nicolson scheme to eliminate the associated stability constraints.

The IBM formulation employs the direct forcing approach first proposed by Uhlmann (2005) and improved by Kempe & Fröhlich (2012*a*). This approach represents the particle using N_L Lagrangian markers with volume $\Delta V_L \approx \Delta V_E$, where ΔV_L is the Lagrangian marker volume and ΔV_E is the volume of each Eulerian grid cell. At each time step, the IBM force, $\boldsymbol{f}_{IBM}$, is calculated as the force required to enforce the difference between the desired velocity $\boldsymbol{u}_d$ at the particle surface and the interpolated velocity from the Eulerian grid. The desired velocity at the particle surface is calculated as the sum of a translational ($\boldsymbol{u}_p$) and a rotational components based on the particle angular velocity vector $\boldsymbol{\omega}_p$ with $\boldsymbol{u}_d = \boldsymbol{u}_p + \boldsymbol{\omega}_p \times \boldsymbol{r}$, where $\boldsymbol{r}$ is the vector pointing from the particle centre of mass to the Lagrangian point. The translational and angular velocities of the particle are then governed by

$$m_p \frac{\mathrm{d}\boldsymbol{u}_p}{\mathrm{d}t} = \rho_f \left[\frac{\mathrm{d}}{\mathrm{d}t} \int_{\Omega_p} \boldsymbol{u} \, \mathrm{d}\Omega_p - \int_S \boldsymbol{f}_{IBM} \, \mathrm{d}S \right] + V_p(\rho_p - \rho_f)\boldsymbol{g} + \boldsymbol{F}_{c,p}, \tag{2.2a}$$

$$I_p \frac{\mathrm{d}\boldsymbol{\omega}_p}{\mathrm{d}t} = \rho_f \left[\frac{\mathrm{d}}{\mathrm{d}t} \int_{\Omega_p} \boldsymbol{r} \times \boldsymbol{u} \, \mathrm{d}\Omega_p - \int_S \boldsymbol{r} \times \boldsymbol{f}_{IBM} \, \mathrm{d}S \right] + \boldsymbol{T}_{c,p}, \tag{2.2b}$$

where the integrals are calculated over the discrete volumes associated with the Lagrangian points given by the surface S and region Ω_p, where m_p is the mass of the particle, $\boldsymbol{g}$ is the gravitational acceleration vector which points in the negative z-direction, V_p is the volume of the particle, ρ_p is the particle density, $\boldsymbol{F}_{c,p}$ and $\boldsymbol{T}_{c,p}$ are the force and torque due to particle–particle and particle–wall interactions and I_p is the moment of inertia of the particle. For a description of each term in (2.2), please refer to the papers by Uhlmann (2005) and Kempe & Fröhlich (2012*a*). Interpolation of variables between the Lagrangian and Eulerian grid employs the discrete delta function kernel proposed by Peskin (1977) and Roma, Peskin & Berger (1999).

The original direct forcing approach proposed by Uhlmann (2005) has two disadvantages: (1) the rigid-body approximation used to approximate the volume integral, $(\mathrm{d}/\mathrm{d}t) \int_{\Omega_p} \rho_f \boldsymbol{u} \, \mathrm{d}\Omega_p$ in (2.2) introduces a singularity at density ratio of $\rho_p/\rho_f = 1$ and stability limit of $\rho_p/\rho_f \approx 1.2$ (Uhlmann 2005; Kempe & Fröhlich 2012*a*); and (2) the explicit calculation of $\boldsymbol{f}_{IBM}$ leads to error that is inversely proportional to Re_p and cannot be eliminated by refining the time step (Kempe & Fröhlich 2012*a*). The restriction associated with the rigid-body approximation is eliminated by introducing the numerical level-set approximation of the volume integral in (2.2) instead of applying the rigid-body approximation. The error associated with $\boldsymbol{f}_{IBM}$ is reduced by applying a heuristic number of outer forcing loops (Wang, Fan & Luo 2008; Kempe & Fröhlich 2012*a*). In each outer forcing loop, the Eulerian velocity field is interpolated between the Eulerian and

https://doi.org/10.1017/jfm.2021.780 Published online by Cambridge University Press

Lagrangian grid and updated with the newly calculated $\boldsymbol{f}_{IBM}$ to satisfy the no-slip boundary condition at the particle surface. Details can be found in the paper by Kempe & Fröhlich (2012*a*), who recommended three outer forcing loops while Biegert *et al.* (2017) recommended one loop based on various validation cases. After validating with different cases, two outer forcing loops were used for the simulations in this study.

To model the forces associated with particle–particle and particle–wall interactions, the total force and torque on particle p due to interaction with $q = 1, 2, \ldots, N_p$ particles and a wall w are computed with

$$\boldsymbol{F}_{c,p} = \sum_{p,q \neq p}^{N_p} (\boldsymbol{F}_{n,q} + \boldsymbol{F}_{t,q}) + \boldsymbol{F}_{n,w} + \boldsymbol{F}_{t,w}, \tag{2.3a}$$

$$\boldsymbol{T}_{c,p} = \sum_{p,q \neq p}^{N_p} R_{p,cp}\boldsymbol{n}_{p,q} \times \boldsymbol{F}_{t,q} + R_{p,cp}\boldsymbol{n}_{p,w} \times \boldsymbol{F}_{t,w}, \tag{2.3b}$$

where $\boldsymbol{F}_{n,q}$ and $\boldsymbol{F}_{t,q}$ are the normal and tangential collision forces between particle p and q; $\boldsymbol{F}_{n,w}$ and $\boldsymbol{F}_{t,w}$ are the normal and tangential collision forces between particle p and a wall; $R_{p,cp}$ is the effective radius between particle p and q; $\boldsymbol{n}_{p,q}$ is the vector normal to the plane of contact between particles p and q; $\boldsymbol{n}_{p,w}$ is the vector normal to the wall at the point of contact with particle q. Normal collision forces $\boldsymbol{F}_{n,q}$ consist of contributions from both lubrication and contact based on the separation distance between the particles (Biegert *et al.* 2017). Collision models usually have high stiffness in which the collision time step size is much smaller than the fluid time step size. To avoid this, we follow the approach by Biegert *et al.* (2017) who employ the collision model proposed by Kempe & Fröhlich (2012*b*).

The code we employ for the simulations in this paper is based on the code developed by Dr Hyungoo Lee and Dr Sivaramakrishnan Balachandar, who employed IBM with the direct forcing approach by Uhlmann (2005) to simulate the near-wall motion of an isolated particle (Lee & Balachandar 2010; Lee *et al.* 2011). We modified their code following improvements to the IBM method suggested by Kempe & Fröhlich (2012*a*) and Biegert *et al.* (2017) as follows. To improve the accuracy of computing fluid–solid interactions, the following modifications were made: (1) a three-step Runge–Kutta time-stepping scheme instead of third-order Adams–Bashforth for the advection terms in (2.1); (2) outer forcing loops to reduce the error associated with explicit calculation of the forcing in the IBM method (Kempe & Fröhlich 2012*a*); (3) higher-order schemes with predictor and corrector steps to discretize the particle motion equations (2.2) (Biegert *et al.* 2017). Because the original code was not designed to simulate particle–particle interactions, collision models based on Kempe & Fröhlich (2012*b*) and Biegert *et al.* (2017) were implemented. Finally, computational performance was made efficient by (1) using appropriate MPI (Open MPI-3.0) structures to transfer Lagrangian and Eulerian information related to particle–particle collisions at interprocessor boundaries and (2) employing HYPRE libraries developed at the Lawrence Livermore National Laboratory (Chow, Cleary & Falgout 1998; Falgout 2006) to solve the linear systems associated with implicit discretization of the viscous terms and the pressure-Poisson equation.

3. Fluidized bed simulation set-up

To simulate the fluidized bed, three-dimensional simulations are conducted with $N_p =$ 2000 particles in the reactor channel shown in figure 1. The particles have a uniform

https://doi.org/10.1017/jfm.2021.780 Published online by Cambridge University Press

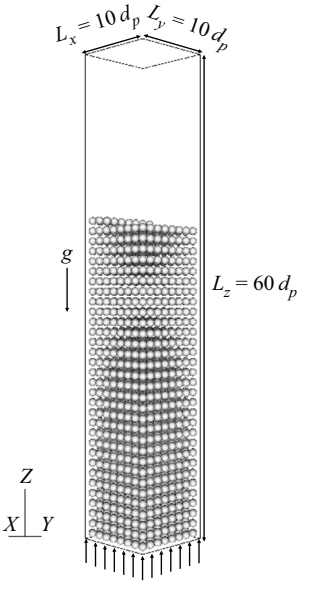


Figure 1. The three-dimensional computational domain, showing the fluidized bed, the uniform inflow velocity profile and the initial particle positions.

diameter $d_p = 2$ mm and density $\rho_p = 1300$ kg m^{-3}, and the fluid has a kinematic viscosity $\nu = 10^{-6}$ m^2 s^{-1} and density $\rho_f = 998.21$ kg m^{-3}, resulting in Archimedes number $Ar = 23\,600$ (Galileo number $Ga = 154$) that is defined as

$$Ar = Ga^2 = \frac{g(s-1)d_p^3}{\nu^2}, \tag{3.1}$$

where $s = \rho_p/\rho_f$ is the ratio of particle to fluid density. The particle collisions have a dry restitution coefficient $e_{dry} = 0.97$ (Foerster *et al.* 1994; Joseph *et al.* 2001), coefficient of kinetic friction $\mu_k = 0.15$ (Joseph & Hunt 2004) and coefficient of static friction $\mu_s = 0.8$ (Dieterich 1972). The grid spacing is uniform in the x, y and z directions and given by $\Delta x = \Delta y = \Delta z = h = d_p/25.6$, which is sufficient to resolve the flow–particle interactions (Biegert 2018; Kempe & Fröhlich 2012*a*). The channel width is given by $L_x = L_y = 10d_p$ and its length is $L_z = 60d_p$, giving a three-dimensional grid with $256 \times 256 \times 1536$ grid points. The time step size is $\Delta t = 1.5 \times 10^{-4}$ s, resulting in a maximum Courant number of 0.5 for the cases with the highest upflow velocities.

The primary parameter of interest is the particle Reynolds number $Re_p = u_0 d_p/\nu$, where the average upflow velocity at the inlet, u_0, is varied to investigate Reynolds number effects. Cases are run with periodicity in the x and y directions. A total of six simulations were conducted with $0.010 \le u_0 \le 0.035$ m s^{-1}, giving $20 \le Re_p \le 70$. For all cases, the pressure is specified at the top boundary as $p = 0$, while at the bottom boundary the inflow velocity is specified as uniform and given by $w(x, y) = u_0$.

Simulations are initialized with a uniform distribution of particles with a spacing of $1d_p$ and the flow is impulsively started from rest. The upflow velocity leads to expansion of the bed and random motion of the particles until statistical equilibrium is reached, at which time the dynamics are independent of the initial particle distribution.

https://doi.org/10.1017/jfm.2021.780 Published online by Cambridge University Press

4. Results and discussion

4.1. Instantaneous and time-average porosity

To understand the time evolution of the particles, we define the ensemble-average instantaneous vertical velocity of particles using the ensemble-average

$$\langle\langle\{\cdot\}\rangle\rangle = \frac{1}{N_p}\sum_{i=1}^{N_p}\{\cdot\}_i, \tag{4.1}$$

where $\{\cdot\}_i$ corresponds to the variable of particle i. As shown in figure 2(a), the ensemble-averaged instantaneous vertical velocity of particles $\langle\langle w_p\rangle\rangle$ initially increases with time as the bed expands because the average drag force on the particles exceeds their submerged weight. Eventually, the average drag is in balance with the submerged weight, leading to statistical equilibrium. Defining the particle turnover time as $\tau_T = d_p/u_0$, simulations are run for $t_{max} = 100$–$300\tau_T$, depending on Re_p, to ensure statistically stationary results. Time-averaged statistics are denoted by the overbar and computed over the last 80 turnover times, such that

$$\overline{\{\cdot\}} = \frac{1}{80\tau_T}\int_{t_0}^{t_{max}}\{\cdot\}\,\mathrm{d}t, \tag{4.2}$$

where $t_0 = t_{max} - 80\tau_T$. Unless otherwise stated, the time-averaging operator has been applied to compute statistically stationary quantities.

In the simulations, the porosity decreases from unity at the inlet, remains relatively constant and then increases to unity at the top of the fluidized bed. Therefore, a spatially variable porosity is expected as compared to the homogeneous porosity in a fluidized bed away from boundaries. Including results from these two regions (top and bottom) would affect the accuracy and convergence of statistical quantities. To determine the region of homogeneous porosity, we define the instantaneous Eulerian volume fraction of the bed, $\phi(\boldsymbol{x}, t)$ and compute the horizontally averaged (x- and y-directions) Eulerian volume fraction of the bed, $\langle\overline{\phi}\rangle_{xy}(z, t)$ as described in Appendix A. Figure 2(b) shows the time-averaged porosity $1 - \langle\overline{\phi}\rangle_{xy}$ as a function of the vertical position z/d_p for $Re_p = 40$. The time-averaged porosity decreases to 0.63 away from the inlet and then increases to 1 at the top of the fluidized bed. To eliminate boundary effects, we define the modified spatial average for fluid variables as

$$\langle\{\cdot\}\rangle_\beta = \frac{1}{N_\beta}\sum_{i=1}^{N_\beta}\{\cdot\}_{ijk}, \tag{4.3}$$

$$\langle\{\cdot\}\rangle_z = \frac{1}{N_z^*}\sum_{k=k_s}^{k_e}\{\cdot\}_{ijk}, \tag{4.4}$$

$$\langle\{\cdot\}\rangle = \frac{1}{N_x N_y N_z^*}\sum_{i,j=1}^{N_x,N_y}\sum_{k=k_s}^{k_e}\{\cdot\}_{ijk}, \tag{4.5}$$

where $\beta = x$ or y represents the horizontal directions, $k_s = z_b/h$ and $k_e = z_t/h$ are the nearest integer of the bottom and top of the fluidized-bed and z_b and z_t are the vertical position of the bottom and top of the homogeneous fluidized bed, respectively.

https://doi.org/10.1017/jfm.2021.780 Published online by Cambridge University Press

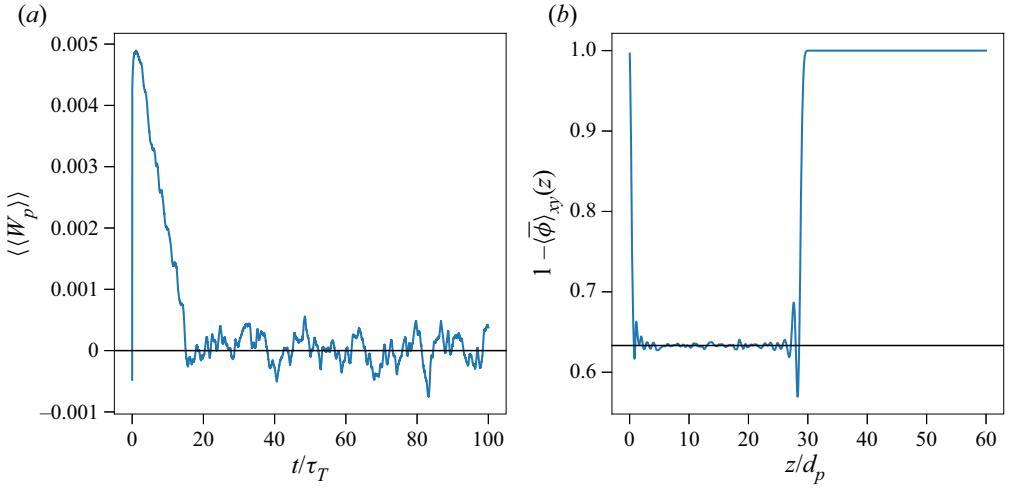


Figure 2. (*a*) Time series of the ensemble-average instantaneous vertical particle velocity $\langle\langle w_p\rangle\rangle$ showing how statistical equilibrium is reached at roughly $t = 20\tau_T$, where $\tau_T = d_p/u_0$ is the particle turnover time and (*b*) vertical variation of time-average porosity $1 - \langle\overline{\phi}\rangle_{xy}$ showing the effects of boundary conditions on the bottom and top of the fluidized bed for the case with $Re_p = 40$.

The modified ensemble-average operator for particle variables is then defined as

$$\langle\{\cdot\}\rangle = \frac{1}{N_p^*}\sum_{i=1}^{N_p}\{\cdot\}_i \mathbf{1}_{z_b<z_p<z_t}(z_p), \tag{4.6}$$

where $N_p^* = \sum_{n=1}^{N_p}\mathbf{1}_{z_b<z_p<z_t}(z_p)$ is the number of particles that are located within the homogeneous fluidized bed, and

$$\mathbf{1}_{z_b<z_p<z_t}(z_p) = \begin{cases} 1, & z_b < z_p < z_t, \\ 0, & \text{otherwise}, \end{cases} \tag{4.7}$$

is the indicator function that describes whether particles are located in the spatially homogeneous region of the fluidized bed.

The relationship between the upflow velocity and volume fraction of particles has been studied extensively (Richardson & Zaki 1954; Garside & Al-Dibouni 1977; Di Felice 1995; Nicolai *et al.* 1995; Di Felice & Parodi 1996; Di Felice 1999; Yin & Koch 2007; Hamid, Molina & Yamamoto 2014; Zaidi *et al.* 2015; Willen & Prosperetti 2019) and is typically described by the power law relationship

$$u^* = \frac{u_0}{w_{ref}} = k(1 - \langle\overline{\phi}\rangle)^n, \tag{4.8}$$

where w_{ref} is the settling velocity of a single particle in the domain of interest, k is a low volume fraction correction (Di Felice 1995, 1999; Di Felice & Parodi 1996; Yin & Koch 2007) and n is the expansion or power law exponent. The settling velocity of a single

https://doi.org/10.1017/jfm.2021.780 Published online by Cambridge University Press

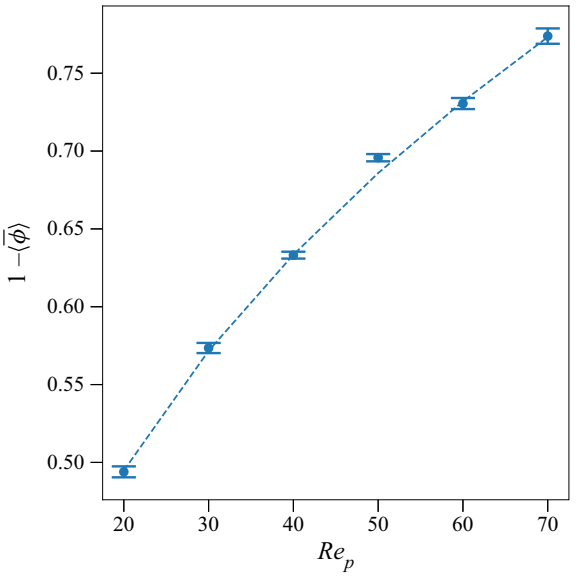


Figure 3. Porosity $1-\langle\overline{\phi}\rangle$ as a function of Re_p for the simulated cases. The dashed lines were constructed based on fitting to the power law equation (4.8).

particle in an infinitely large domain, w_{ref}, is computed with (Yin & Koch 2007)

$$Ar = \begin{cases} 18Re_t\left[1+0.1315Re_t^{(0.82-0.05\log_{10}Re_t)}\right], & 0.01 < Re_t < 20, \\ 18Re_t\left[1+0.1935Re_t^{0.6305}\right], & 20 < Re_t < 260, \end{cases} \tag{4.9}$$

where $Re_t = w_{ref}d_p/\nu$ and $Ar = (\rho_p/\rho_f - 1)gd_p^3/\nu^2$ is the Archimedes number. In this work, $Ar = 2.36\times10^4$ giving $Re_t \approx 200$ which is within the range of (4.9). The error of (4.9) has been shown to range from 2 % to 4 % (Yin & Koch 2007; Willen & Prosperetti 2019). Fitting our results to (4.8) yields values of $k = 0.72$ and $n = 2.82$ that are consistent with published values (Yin & Koch 2007; Willen & Prosperetti 2019). In this paper we focus on the relationship between the porosity $1-\langle\overline{\phi}\rangle$ and Re_p shown in figure 3, which also includes the power-law fits and shows that the porosity increases with increasing Re_p.

4.2. *Kinematic wave speed*

As discussed by many researchers (Ham & Homsy 1988; Duru *et al.* 2002; Sundaresan 2003; Derksen & Sundaresan 2007), as Re_p increases above $Re_{mf} = u_{mf}d_p/\nu$ where Re_{mf} is the minimum fluidization Reynolds number, particles start to expand and upward-propagating waves can be observed. Below an intermediate Re_p, stable and neutral wave modes exist in which the amplitude of the waves decreases and remains approximately constant. For larger Re_p, unstable wave modes develop in which the wave amplitude grows with height, leading to large fluctuations in porosity. Zenit & Hunt (2000) investigated the time evolution of the ensemble- and time-averaged porosity $1-\langle\overline{\phi}\rangle$ and concluded that large-amplitude, low-frequency fluctuations dominated at low porosity (high volume fraction $\phi > 0.3$) and small-amplitude, high-frequency fluctuations dominated at high porosity (low volume fraction $\phi < 0.3$).

Figure 4(*a–c*) show two-dimensional z–t plots of the volume fraction fluctuation $\langle\phi\rangle'_{xy} = \langle\phi\rangle_{xy} - \langle\overline{\phi}\rangle_{xy}$. Waves can be identified visually but are difficult to quantify due

https://doi.org/10.1017/jfm.2021.780 Published online by Cambridge University Press

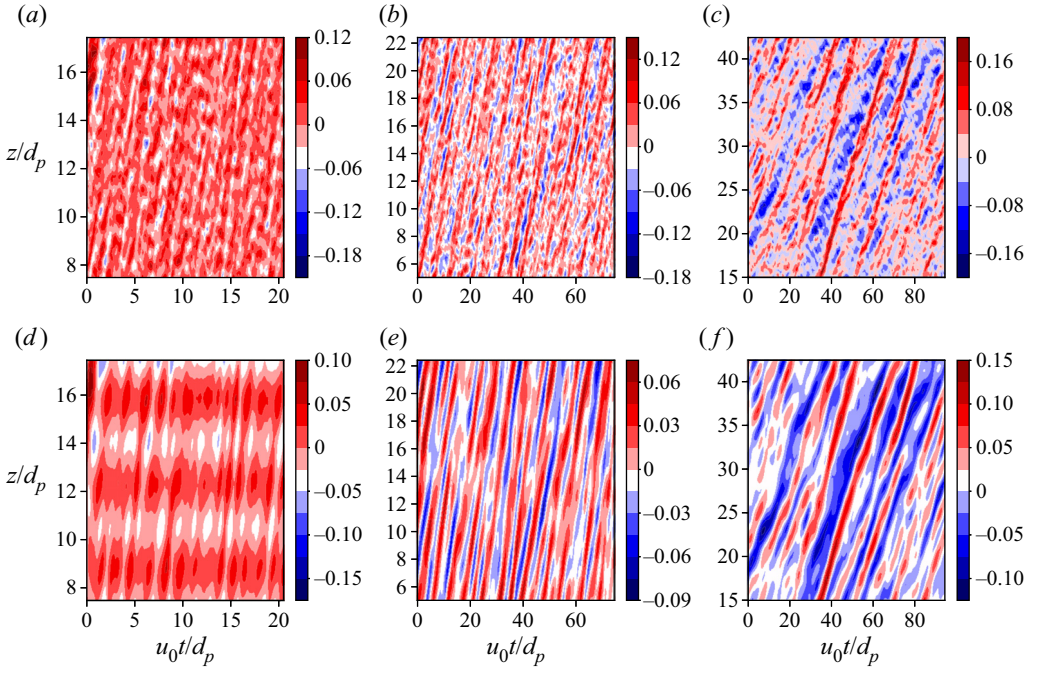


Figure 4. Volume fraction fluctuation $\langle\phi\rangle'_{xy}$ as a function of time u_0t/d_p and vertical position z/d_p for the cases with $Re_p = 20$, 40 and 70 in panels (a,d), (b,e) and (c,f), respectively. Panels (d–f) represent the low wavenumber motions with wavenumber $k_z < k_{z,thresh}$.

to the presence of noise and superposition of waves with different modes. Researchers have reported that $\langle\phi\rangle'_{xy}$ can be classified based on frequencies (Zenit & Hunt 2000) or wavenumber (Willen *et al.* 2017). To separate low-wavenumber waves from the raw data, we modified the Fourier reconstruction method proposed by Willen *et al.* (2017) by defining low-wavenumber fluctuations for $k_z < k_{z,thresh}$, where $k_{z,thresh} = (z_t - z_b)/2d_p$ is the threshold wavenumber. Since the behaviour of small spatial-scale fluctuations ($k_z \geq k_{z,thresh}$) is an artefact of the spatial averaging, therefore, this study only focuses on the large-scale fluctuations ($k_z < k_{z,thresh}$) which allow interpretation of kinematic wave behaviour. Figure 4(d–f) show the low-wavenumber $\phi'_{k_z<k_{z,thresh}}$. In general, upward-propagating waves are clearly observed with alternating regions of high and low porosity for $k_z < k_{z,thresh}$. For $Re_p = 20$ (figure 4d), $\phi'_{k_z<k_{z,thresh}}$ is a strong function of vertical position z in which $\phi'_{k_z<k_{z,thresh}}$ varies over a distance of $\sim 2d_p$ and depends weakly on time. For $Re_p > 20$, wave motion is dependent both on time and vertical position.

The wave-like motions can be represented by a superposition of different waves with normalized wavenumber $k^* = kd_p$ and normalized frequency $\omega^* = \omega d_p/u_0$. Figure 5($a$–$c$) show the $\langle\phi\rangle'_{xy}$ in spectral space as a function of k^* and ω^*. Overall, $\langle\phi\rangle'_{xy}$ is dominated by low wavenumber waves with $k^* \approx 1$ and the dominant frequency ω^* decreases as Re_p increases. At $Re_p = 20$, regions of high $k^* - \omega^*$ can be observed even though the spectral density is relatively small. This illustrates that high-frequency wave modes are more significant at low Re_p than high Re_p. As Re_p increases, different modes collapse into a linear relationship. Figure 5(d–f) show the $k^* - \omega^*$ spectra of $\phi'_{k_z<k_{z,thresh}}$. For $\phi'_{k_z<k_{z,thresh}}$, by eliminating high wavenumber modes, different modes of waves collapse into a line

https://doi.org/10.1017/jfm.2021.780 Published online by Cambridge University Press

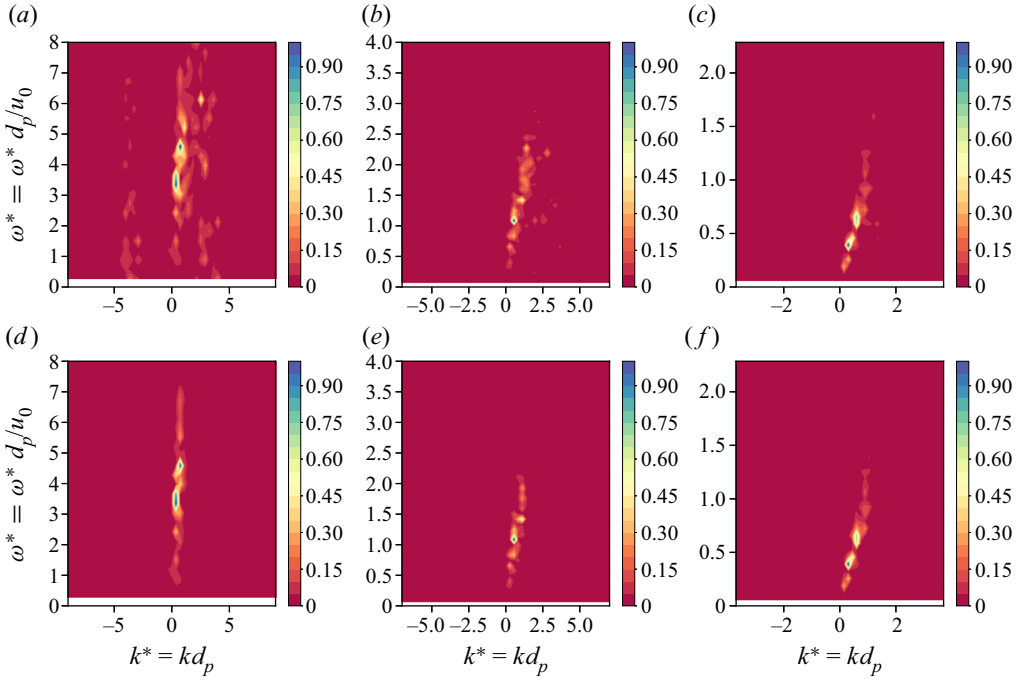


Figure 5. Energy spectra of volume fraction fluctuation $\langle\phi\rangle'_{xy}$ as a function of normalized wavenumber k^* and normalized frequency ω^* for the cases with $Re_p = 20$, 40 and 70 in panels (a,d), (b,e) and (c,f), respectively, and with ϕ' and $\phi'_{k_z<k_{z,thresh}}$ in panels (a–c) and (d–f), respectively.

and a wave speed can be estimated from the kinematic relationship $\omega = ck$ using linear regression.

To demonstrate the existence of kinematic waves in the fluidized bed, we employ the model proposed by Wallis (2020) which relates volume fraction to wave speed with

$$c = kn\langle\overline{\phi}\rangle(1 - \langle\overline{\phi}\rangle)^{n-1}w_{ref}, \tag{4.10}$$

where c is wave speed and other variables are defined in (4.8). To calculate the wave speed, we employ the two-dimensional autocorrelation approach as demonstrated by Yao, Criddle & Fringer (2021*a*) and Yao *et al.* (2021*b*). The autocorrelation of reconstructed volume fraction fluctuation $\phi'_{k_z<k_{z,thresh}}$ is computed and wave speeds are calculated as the slope. As shown in figure 6, the calculated wave speeds are in agreement with the modelled values. The difference between the calculated wave speeds and modelled values are likely due to the dispersive effects, which are not considered in (4.10) (Shajahan & Breugem 2020; Wallis 2020).

4.3. *Velocity fluctuations*

In a fluidized bed, the ensemble-averaged vertical velocity $\langle\langle w\rangle\rangle = 0$, indicating a balance between the submerged weight of the particles and the drag force. However, many researchers have reported that the velocity fluctuations can be as high as 10 %–170 % of the superficial velocity u_0 depending on the volume fractions (Nicolai *et al.* 1995; Hamid *et al.* 2014; Zaidi *et al.* 2015; Willen & Prosperetti 2019). To understand the effect of Re_p

https://doi.org/10.1017/jfm.2021.780 Published online by Cambridge University Press

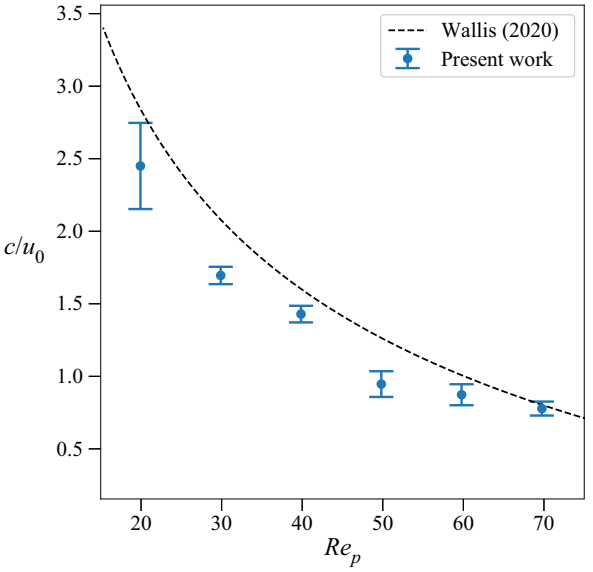


Figure 6. Wave speed based on the autocorrelation as a function of the particle Reynolds number Re_p.

on the velocity fluctuations, we computed the root mean square velocity fluctuation

$$u_{rms,\alpha} = \overline{\sqrt{\langle u'_\alpha u'_\alpha \rangle}}, \tag{4.11}$$

where $u'_\alpha = u_\alpha - \langle \overline{u} \rangle_\alpha$ is the particle velocity fluctuation and $\alpha = x$, y or z. Here, the overbar is the time average defined in (4.2) and the angle brackets $\langle \cdot \rangle$ imply an ensemble average over particles in the homogeneous region of the fluidized bed as defined in (4.6). Figure 7 shows $u_{rms,\alpha}$ normalized by u_0 as a function of Re_p. Both $u_{rms,x}$ and $u_{rms,z}$ increase initially and reach a maximum at $Re_p \approx 40$ and then decrease with increasing Re_p. Defining the anisotropy as $u_{rms,z}/u_{rms,x}$, for the range of Re_p simulated, the anisotropy ranges between 1.7 and 1.8. Similar trends were observed by Willen & Prosperetti (2019). While a maximum in velocity fluctuations is expected because they should be zero for both a single particle ($\phi \approx 0$) and a packed bed ($\phi \approx 0.6$), the physical mechanisms leading to a maximum at $Re_p \approx 40$ have not been reported in the literature.

In addition to particle velocity fluctuations, the fluid velocity fluctuations in the vicinity of the particles are also quantified. Many methods have been proposed to quantify the fluid velocity in the vicinity of the particles (Bagchi & Balachandar 2003; Kidanemariam *et al.* 2013; Uhlmann & Doychev 2014). In this study, we adopted the approach by Kidanemariam *et al.* (2013) where the fluid velocity in the vicinity of the particles is defined as the fluid in a spherical volume of diameter $2d_p$ where the centre of the spherical volume coincides with the particle centre. Figure 8 shows the fluid velocity fluctuations as a function of Re_p. Overall, the trends are very similar to the particle velocity fluctuations in figure 7. However, the magnitudes are smaller, indicating weaker fluid velocity fluctuations compared with the particles. It is likely that the interparticle collisions leading to the particle velocity fluctuations occur over time scales that are too short for the fluid to respond, resulting in lower fluid velocity fluctuations.

https://doi.org/10.1017/jfm.2021.780 Published online by Cambridge University Press

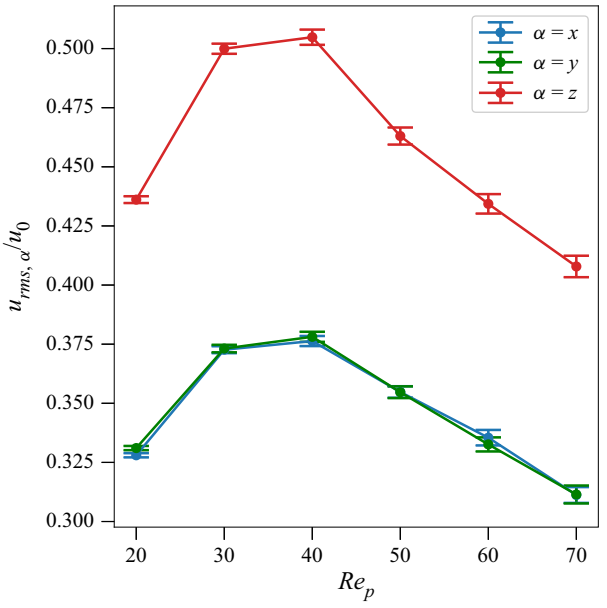


Figure 7. The root mean square velocity fluctuation normalized by the superficial velocity u_0 as a function of the particle Reynolds number Re_p.

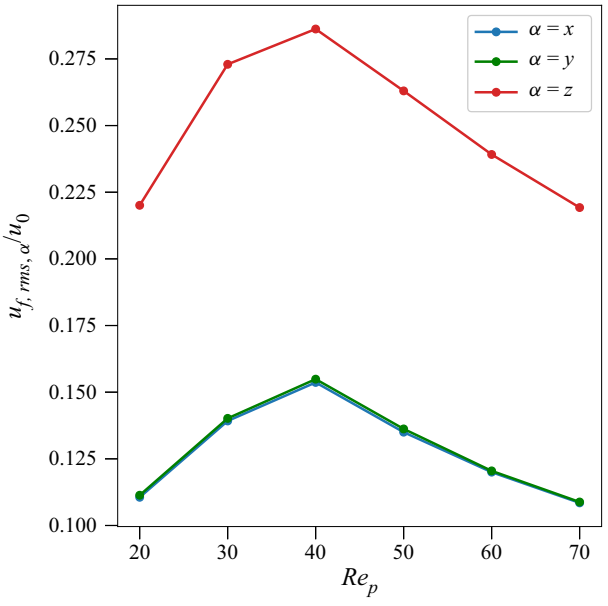


Figure 8. The root mean square fluid velocity fluctuation in vicinity to particles normalized by the superficial velocity u_0 as a function of the particle Reynolds number Re_p.

4.4. *Autocorrelation and pairwise distributions*

To understand the processes governing the fluctuating particle motions, we compute the instantaneous velocity fluctuation autocorrelation for a given time lag τ:

$$R_{\alpha\alpha}(\tau) = \frac{\langle u'_\alpha(t_0)u'_\alpha(t_0+\tau)\rangle}{\langle u'_\alpha(t_0)u'_\alpha(t_0)\rangle}; \tag{4.12}$$

https://doi.org/10.1017/jfm.2021.780 Published online by Cambridge University Press

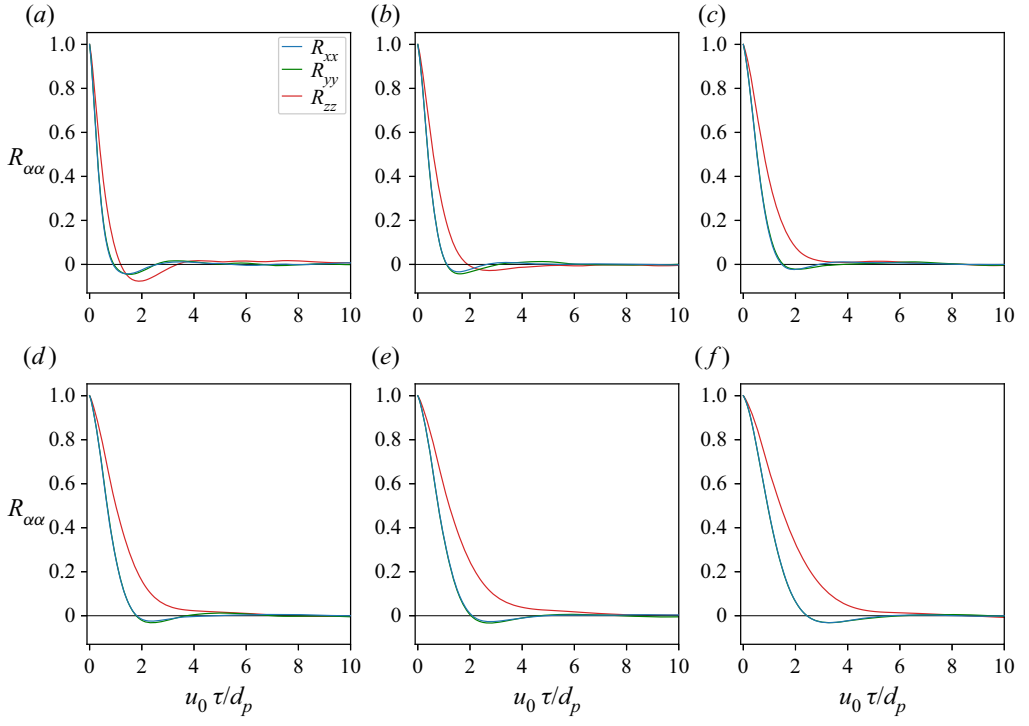


Figure 9. Transverse (R_{xx}, R_{yy}) and axial (R_{zz}) velocity fluctuation autocorrelation as a function of the lag time τ (equation (4.12)) with different particle Reynolds numbers Re_p. (*a*) $Re_p = 20$, (*b*) 30, (*c*) 40, (*d*) 50, (*e*) 60, (*f*) 70.

the results are shown in figure 9. For all Re_p, the transverse velocity fluctuations (R_{xx}, R_{yy}) for $1 < u_0\tau/d_p < 6$ indicate regimes of anticorrelation, the extent of which decreases with increasing Reynolds number. The axial velocity fluctuations R_{zz} decorrelate monotonically to zero except for $Re_p = 20$ and 30 where a region of anticorrelation exists. In addition, the transverse velocity fluctuations decorrelate faster than the axial velocity fluctuations because of preferential excitation of random particle motions in the axial direction by the axial flow. Similar results have been reported by previous three-dimensional simulations and experimental results with different particle properties (Nicolai *et al.* 1995; Esteghamatian *et al.* 2017; Willen & Prosperetti 2019).

The decorrelation time for the α component of the velocity fluctuations can be quantified by the true integral time scale

$$\mathcal{T}_{\alpha,\infty} = \int_0^\infty R_{\alpha\alpha}(\tau)\,\mathrm{d}\tau\,. \tag{4.13}$$

However, in simulations where data is limited, the computed integral time scale is instead approximated with

$$\mathcal{T}_{\alpha,cal} = \int_0^{t_f} R_{\alpha\alpha}(\tau)\,\mathrm{d}\tau, \tag{4.14}$$

where t_f is the simulation time and $N_\tau = u_0 t_f/d_p$ is the non-dimensional time to calculate the computed integral time scale.

Figure 10 shows that the magnitude of $\mathcal{T}_{\alpha,cal}$ increases initially as a function of N_τ and fluctuates about a mean value due to the presence of wave-like autocorrelations.

https://doi.org/10.1017/jfm.2021.780 Published online by Cambridge University Press

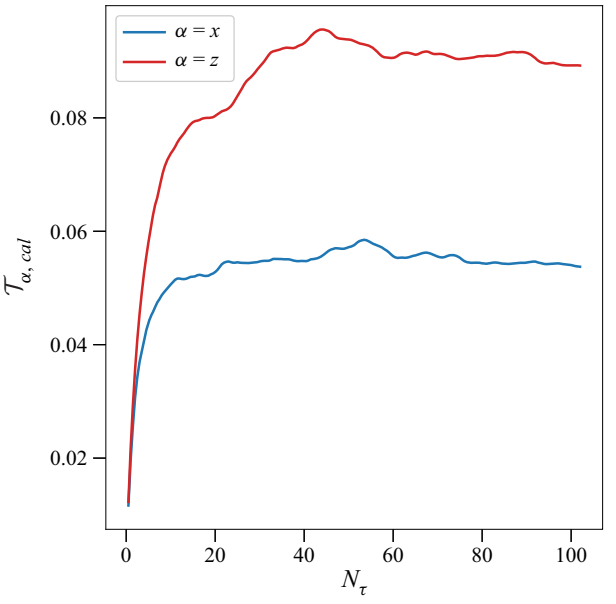


Figure 10. Computed integral time scale $\mathcal{T}_{\alpha,cal}$ as a function of N_τ.

Similar wave-like autocorrelations were observed by Esteghamatian *et al.* (2017) and Nicolai *et al.* (1995). To quantify the error associated with the computed integral time scale, we computed the mean and standard deviation of $\mathcal{T}_{\alpha,cal}$ as

$$\mathbb{E}(\mathcal{T}_{\alpha,cal}) = \frac{1}{N_\tau - N_{\tau,thresh}} \sum_{i=N_{\tau,thresh}}^{N_\tau} \mathcal{T}^i_{\alpha,cal}, \tag{4.15}$$

$$\sigma(\mathcal{T}_{\alpha,cal}) = \sqrt{\mathbb{E}(\mathcal{T}^2_{\alpha,cal}) - \mathbb{E}(\mathcal{T}_{\alpha,cal})^2}, \tag{4.16}$$

where $N_{\tau,thresh}$ is the minimum N_τ for $\mathcal{T}_{\alpha,cal}$ to reach equilibrium, and $\mathbb{E}(\mathcal{T}_{\alpha,cal})$ and $\sigma(\mathcal{T}_{\alpha,cal})$ are the mean and standard deviation of the calculated integral time scale, respectively.

Figure 11 shows the effect of Re_p on $\mathbb{E}(\mathcal{T}_{\alpha,cal})$ and the ratio $\mathbb{E}(\mathcal{T}_{x,cal})/\mathbb{E}(\mathcal{T}_{z,cal})$, which is a measure of system anisotropy. Overall, $\mathbb{E}(\mathcal{T}_{z,cal}) > \mathbb{E}(\mathcal{T}_{x,cal})$ for the range of Re_p simulated, implying $\mathbb{E}(\mathcal{T}_{x,cal})/\mathbb{E}(\mathcal{T}_{z,cal}) < 1$. This is consistent with the fact that the axial velocity fluctuations take longer to decorrelate owing to the presence of the mean flow (Nicolai *et al.* 1995; Willen & Prosperetti 2019; Esteghamatian *et al.* 2017). Interestingly, a minimum anisotropy (maximum of $\mathbb{E}(\mathcal{T}_{x,cal})/\mathbb{E}(\mathcal{T}_{z,cal})$) and maximum anisotropy (minimum of $\mathbb{E}(\mathcal{T}_{x,cal})/\mathbb{E}(\mathcal{T}_{z,cal})$) are observed at $Re_p = 40$ and 50, indicating the most and least efficient momentum transfer, respectively. In addition, a sharp decrease in $\mathbb{E}(\mathcal{T}_{x,cal})/\mathbb{E}(\mathcal{T}_{z,cal})$ is observed as Re_p increases from 40 to 50. This is due to the presence of competing mechanisms related to flow and particle physics, as discussed below.

We computed the normalized autocorrelation length scale, $\ell^*_\alpha = \ell_\alpha/d_p = u_{rms,\alpha}\mathbb{E}(\mathcal{T}_{\alpha,cal})/d_p$ which is a measure of the distance over which particle velocity fluctuations are still correlated, as shown in figure 12(*a*). When the particle velocity fluctuations are dominated by collisions when the porosity is low, the effects

https://doi.org/10.1017/jfm.2021.780 Published online by Cambridge University Press

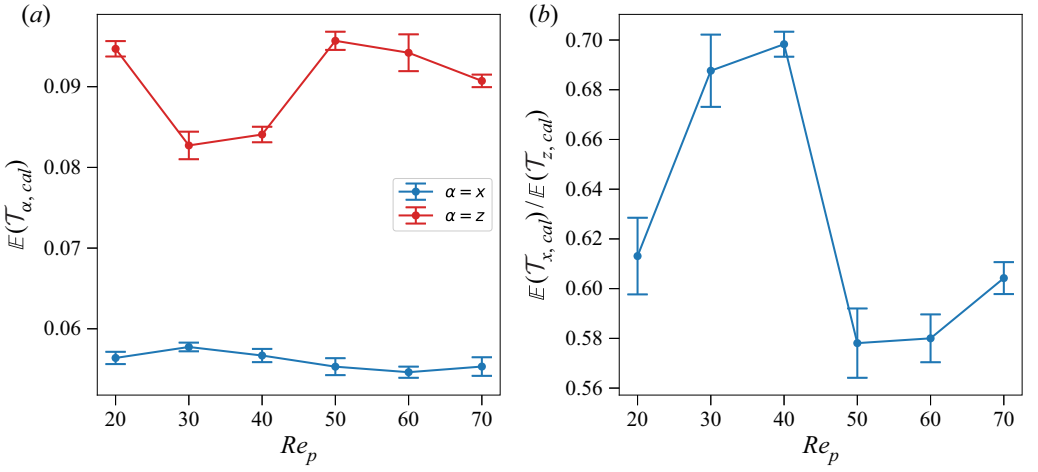


Figure 11. (*a*) The average integral time scales and (*b*) ratio of transverse integral time scale $\mathbb{E}(\mathcal{T}_{x,cal})$ to axial integral time scale $\mathbb{E}(\mathcal{T}_{z,cal})$ as a function of Reynolds number Re_p.

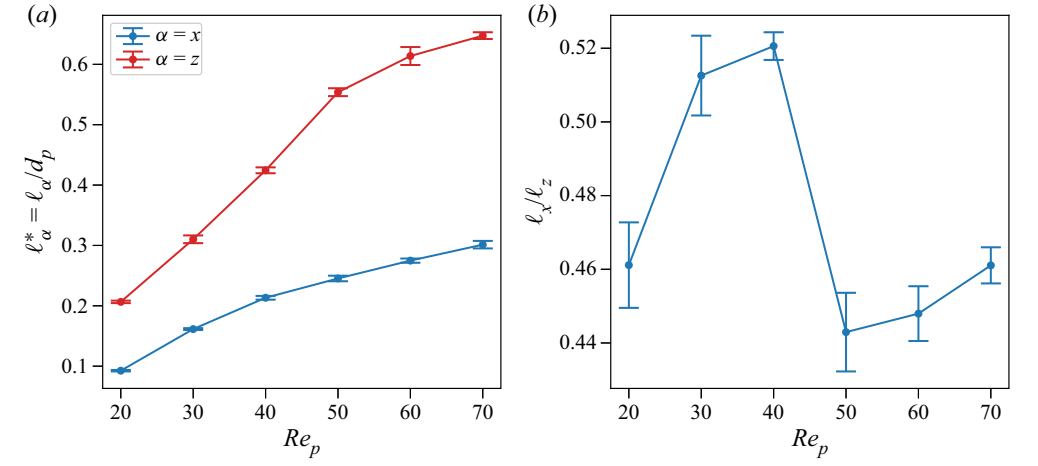


Figure 12. Effect of particle Reynolds number on (*a*) the autocorrelation distance $\ell^*_\alpha = \ell_\alpha/d_p$ and (*b*) ratio of transverse to axial autocorrelation distance ℓ_x/ℓ_z.

of velocity fluctuations do not propagate by more than the particle diameter, and thus $\ell^*_\alpha < 1$. However, when $\ell^*_\alpha > 1$ the particle velocity fluctuations are dominated by the effects of the mean flow on each particle since the effects of velocity fluctuations propagate farther than a particle diameter. For all cases, both ℓ^*_x and ℓ^*_z are less than 1 indicating the particle velocity fluctuations are restricted by the relatively low porosity. Nicolai *et al.* (1995) reported $\ell^*_z > 1$ for particle suspension in the Stokes regime, while Esteghamatian *et al.* (2017) reported $\ell^*_z < 1$. We also computed ℓ_x/ℓ_z which indicates anisotropy. As shown in figure 12(*b*), the anisotropy is maximized at $Re_p = 40$ and decreases sharply between $Re_p = 40$ and $Re_p = 50$, indicating an increase in the anisotropy. This agrees with figure 11(*b*) where a sharp decrease is also observed from $Re_p = 40$ to $Re_p = 50$.

To highlight the different particle Reynolds number regimes leading to the anisotropy, we adapt the pairwise-probability density function from Yin & Koch (2008), which is

https://doi.org/10.1017/jfm.2021.780 Published online by Cambridge University Press

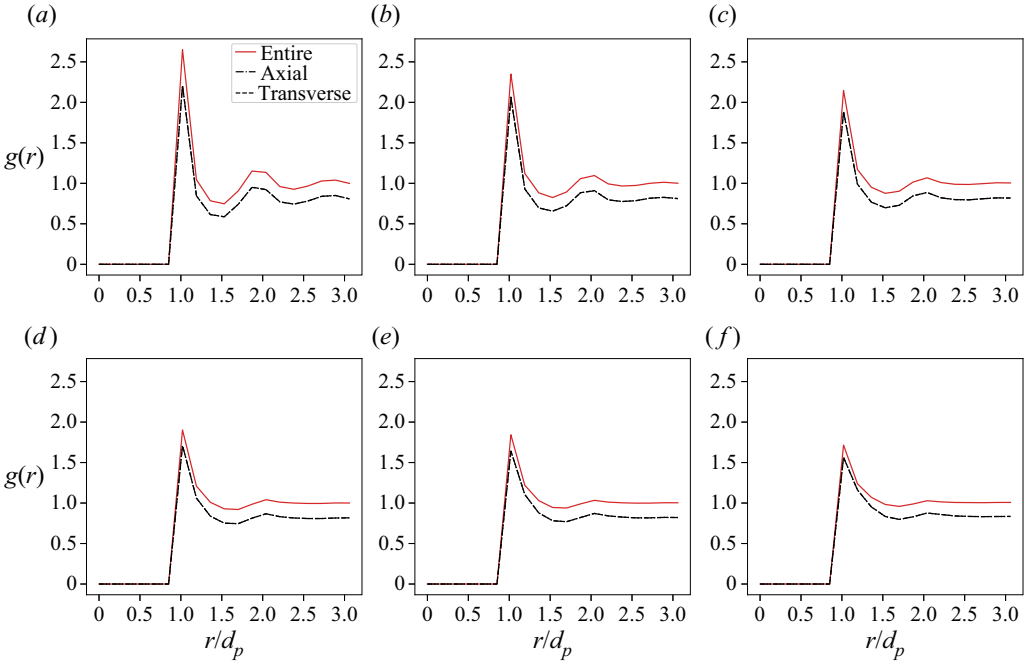


Figure 13. The pairwise distribution function, $g(r,\theta)$ ((4.17)) averaged over three ranges for the simulated cases with different Re_p: (*a*) $Re_p = 20$; (*b*) $Re_p = 30$; (*c*) $Re_p = 40$; (*d*) $Re_p = 50$; (*e*) $Re_p = 60$; (*f*) $Re_p = 70$.

given by

$$g(r,\theta) = g(\boldsymbol{r}) = \frac{L_x L_y L_b}{d_p^3 N_p^2} \left\langle \sum_{i=1}^{N_p} \sum_{j=1, j\neq i}^{N_p} \delta(\boldsymbol{r} - \boldsymbol{r}_{ij}) \right\rangle, \tag{4.17}$$

where $L_b = z_t - z_b$ is the height of the bed where the porosity is homogeneous, δ is defined as

$$\delta(\boldsymbol{r} - \boldsymbol{r}_{ij}) = \begin{cases} 1, & \boldsymbol{r} = \boldsymbol{r}_{ij}, \\ 0, & \text{otherwise} \end{cases} \tag{4.18}$$

and $\boldsymbol{r}_{ij} = [r_{ij}, \theta_{ij}]$ is the position vector between the centre of particle i, $\boldsymbol{x}_i$, and particle j, $\boldsymbol{x}_j$. In cylindrical polar coordinates, $r_{ij} = \|\boldsymbol{x}_i - \boldsymbol{x}_j\|$ is the magnitude of $\boldsymbol{r}_{ij}$ and

$$\theta_{ij} = \begin{cases} \cos^{-1}[(|z_i - z_j|)/r_{ij}] & \text{if } z_i - z_j < 0, \\ \sin^{-1}[(|z_i - z_j|)/r_{ij}] & \text{if } z_i - z_j \geq 0. \end{cases} \tag{4.19}$$

We also compute the pairwise-probability distribution function or radial distribution function as the angular average of $g(r,\theta)$ over three ranges: the entire range ($0 \leq \theta \leq \pi/2$); an effective axial range ($0 \leq \theta \leq \pi/12$); and an effective transverse range ($5\pi/12 \leq \theta \leq \pi/2$). As shown in figure 13, the difference between the transverse and axial radial distribution functions is a measure of the particle arrangement preferences. The results indicate that particles do not have a preferred arrangement over the Re_p simulated, which is likely because the volume fractions we simulate are too large (Yin & Koch 2007; Willen & Prosperetti 2019). At $r/d = 1$ and $r/d = 2$, there is an obvious

https://doi.org/10.1017/jfm.2021.780 Published online by Cambridge University Press

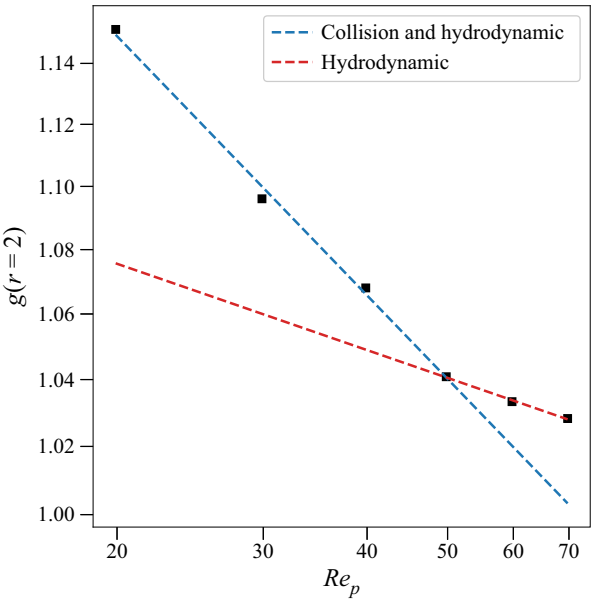


Figure 14. The radial distribution function at $r = 2$, $g(r = 2, \theta)$, averaged over $0 \leq \theta \leq \pi/2$, for ranges of Re_p simulated, with different regimes indicated by the lines obtained through linear regression.

increase in the magnitude of the radial distribution function indicated by peaks in $g(r)$, an effect that decreases with increasing particle Reynolds number (see figure 14). This indicates that particles are more likely to appear at these two locations. Comparing with the three-dimensional simulations by Willen & Prosperetti (2019), in which the peak in the transverse $g(r)$ is slightly higher than the peak in the axial $g(r)$ (implying that a transverse arrangement of particle pairs is slightly favoured over an axial arrangement), we found no difference between the transverse and axial arrangements. A possible explanation of this observation is due the higher Re_t simulated in which the effect of collisions is more prominent. As a result, momentum is transferred more efficiently from the axial to transverse directions, inducing higher transverse velocity fluctuations and disrupting the arrangement of transverse particle pairs observed by Willen & Prosperetti (2019).

To further understand the effect of the particle Reynolds number, figure 14 shows the effect of Re_p on $g(r/d_p = 2)$. For the cases simulated, two regimes can be identified with regressions having correlation coefficients $R^2 > 0.99$. In general, the peak decreases with increasing Reynolds number, although the slope depends on two distinct flow regimes, which are referred to as regime 1 ($Re_p < 50$) and regime 2 ($Re_p \geq 50$) in what follows.

4.5. *Particle–particle and fluid–particle interactions*

The mechanisms dictating the particle velocity fluctuations described in § 4.4 can be explained through analysis of the magnitude of stresses related to the particle–particle and particle–fluid interactions. The role of particle–particle collisions is to transfer momentum from the axial direction to the transverse direction, resulting in a more isotropic system (Esteghamatian *et al.* 2017). To quantify the magnitude of the stress induced by collisions and flow, we computed the normal contact stress, $\sigma_{col,\alpha}$, normal lubrication stress, $\sigma_{lub,\alpha}$, and hydrodynamic stress due to the fluid, $\sigma_{hydro,\alpha}$, as a function of the vertical

https://doi.org/10.1017/jfm.2021.780 Published online by Cambridge University Press

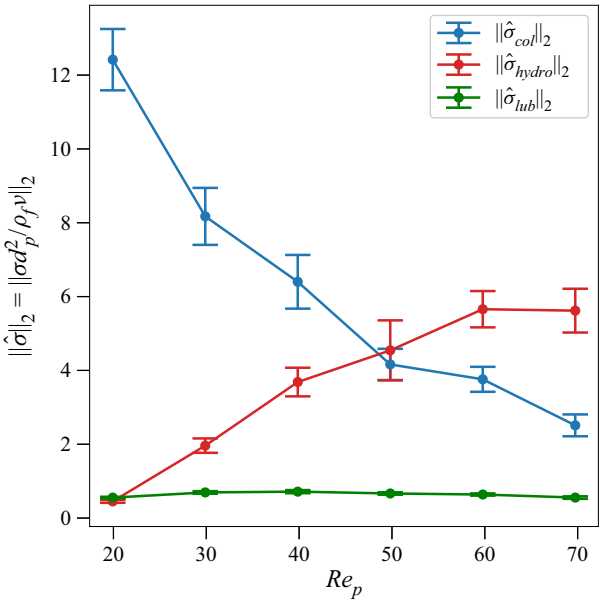


Figure 15. The computed normal contact stress, normal lubrication stress and hydrodynamic stress as a function of particle Reynolds number Re_p.

position in the fluidized bed. The lubrication stress is considered separately from collision and hydrodynamic stresses since both fluid–particle and particle–particle interaction are involved. A detailed derivation of these stresses can be found in Appendix B. All stresses are normalized by $d_p^2/\rho_f \nu^2$ and denoted as $\hat{\sigma}$.

Overall, all the stresses fluctuate about a mean value away from the top and bottom boundaries of the fluidized bed. To quantify the effect of Re_p on each component of the stress, we computed the vertical average of each stress first using the averaging operator defined in (4.3) and then computing the ℓ^2 norm of the stress vector $\boldsymbol{\sigma}$ as $\|\boldsymbol{\sigma}\|_2$. Figure 15 shows the magnitude of the normalized mean stresses as a function of Re_p. As Re_p increases, the effect of $\|\boldsymbol{\sigma}_{col}\|_2$ decreases while the effect of $\|\boldsymbol{\sigma}_{hydro}\|_2$ increases. Both Zenit *et al.* (1997) and Derksen & Sundaresan (2007) have found $\|\boldsymbol{\sigma}_{col}\|_2$ decreases with decreasing ϕ beyond a critical volume fraction. The effect of $\|\boldsymbol{\sigma}_{lub}\|_2$ is negligible, which also agrees with Derksen & Sundaresan (2007) who showed that the lubrication stress is negligible even though the simulated porosity and particle properties are different.

Comparing the magnitude of each stress (figure 15), at $Re_p = 20$ where $\|\boldsymbol{\sigma}_{col}\|_2 \gg \|\boldsymbol{\sigma}_{hydro}\|_2$, collisions dominate over hydrodynamic effects and hydrodynamic effects are negligible. For $20 < Re_p < 40$, as Re_p increases, hydrodynamic effects increase, $\|\boldsymbol{\sigma}_{col}\|_2 > \|\boldsymbol{\sigma}_{hydro}\|_2$ still persists but the difference is decreasing. In this regime, collisions still dominate over hydrodynamic effects but the relative importance of hydrodynamic effects increases. This corresponds to regime 1 in figure 14 where both collisions and hydrodynamics are important in inducing velocity fluctuations. For $Re_p > 40$, $\|\boldsymbol{\sigma}_{hydro}\|_2 > \|\boldsymbol{\sigma}_{col}\|_2$ indicates hydrodynamic effects dominating over collisions, corresponding to regime 2 identified in figure 14. By comparing with results from Yao *et al.* (2021*a*) for simulations of fluidized beds with Archimedes number of 8600 and 13 660 (figure 16), we observe that the critical volume fraction (inversely proportional to particle Reynolds number) decreases as the Archimedes number increases.

https://doi.org/10.1017/jfm.2021.780 Published online by Cambridge University Press

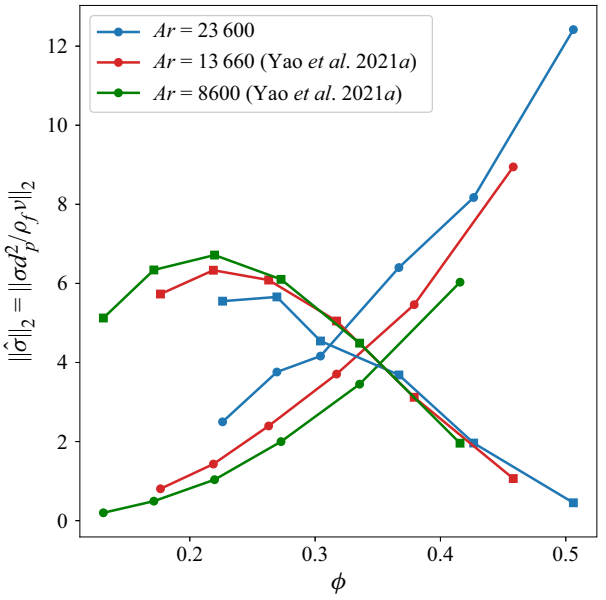


Figure 16. The computed normal contact stress (circle) and hydrodynamic stress (square) as a function of volume fraction ϕ for Archimedes numbers of 8600, 13 660 and 23 600.

However, future work is required to establish a relationship between the optimum particle Reynolds number and a wider range of Archimedes numbers.

The decreasing importance of the collisional stress with increasing Re_p occurs because of a reduction in the collision frequency with increasing Re_p. We define a collision between two particles as occurring when the separation distance between the particle centres is less than the particle diameter d_p. If the number of times particle i collides with another particle during a simulation time step n is given by $N_{c,i}^n$, then the time- and ensemble-average collision frequency is given by

$$\langle \overline{f_c} \rangle = \frac{1}{N_p(t_{max} - t_0)} \sum_{n=n_0}^{n_{max}} \sum_{i=1}^{N_p} N_{c,i}^n, \tag{4.20}$$

where $n_0 = t_0/\Delta t$ and $n_{max} = t_{max}/\Delta t$. Since the porosity and in turn the spacing between particles increases with increasing Re_p (figure 3), the likelihood of collisions should decrease with increasing Re_p, leading to the monotonically decreasing dependence of $\langle \overline{f_c} \rangle$ on Re_p as shown in figure 17(*a*). When the porosity is smaller, the likelihood of collision between particles is higher.

For the simulated cases, the collision frequency as defined in (4.20) is overestimated for small Re_p because particles may interact without colliding and producing a measurable collisional stress. To restrict collisions to those with appreciable normal contact velocities, we define the collision Stokes number with impact velocity u_{imp} as

$$St_{imp} = \frac{u_{imp}\rho_p d_p}{9\rho_f \nu}, \tag{4.21}$$

where u_{imp} is the normal component of the relative particle velocities contacting one another. The effective collision frequency, $\langle \overline{f_c} \rangle_{eff}$, is then computed by including collisions for which $St_{imp} > St_{thresh}$, where St_{thresh} is a threshold Stokes number. The threshold

https://doi.org/10.1017/jfm.2021.780 Published online by Cambridge University Press

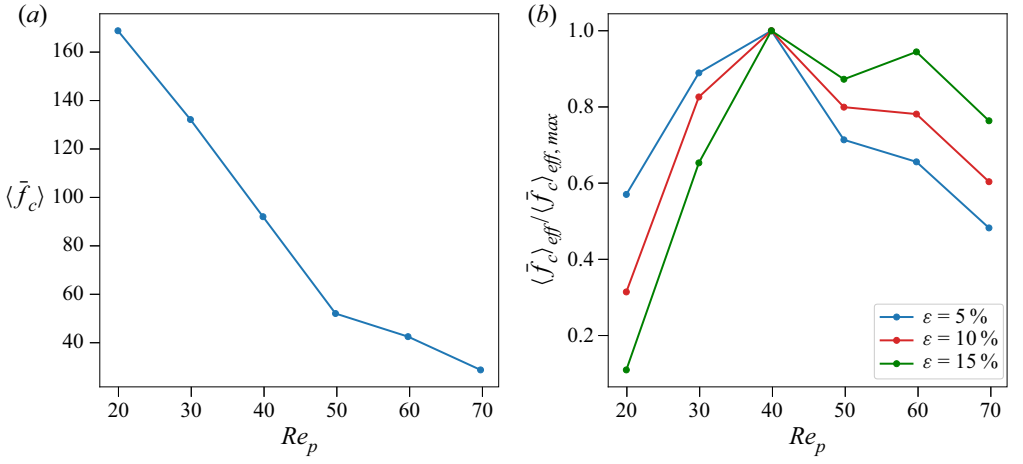


Figure 17. Time- and ensemble-averaged (*a*) collision frequency $\langle \bar{f}_c \rangle$ and (*b*) effective collision frequency $\langle \bar{f}_c \rangle_{eff}$ as a function of particle Reynolds number with different ε.

Stokes number is determined by setting a minimum rebound velocity with an empirical function relating the restitution coefficient to the Stokes number. Defining the velocity of a particle before it is subjected to lubrication and contact forces as $w_{t,\infty}$, the restitution coefficient is given by

$$\varepsilon = \frac{u_{rebound}}{u_{t,\infty}} = \varepsilon_{max} \exp\left(-\frac{30}{St_\infty}\right). \tag{4.22}$$

Here, $\varepsilon_{max} \approx 0.91$ is the maximum restitution coefficient when $St_\infty \to \infty$ (Legendre *et al.* 2006), where

$$St_\infty = \frac{u_{t,\infty} d_p \rho_p}{9 \rho_f \nu_f}. \tag{4.23}$$

In this work, since $u_{t,\infty}$ is difficult to quantify due to simultaneous collisions with the soft-sphere modelling approach, we rearrange (4.22) to relate St_{imp} to ε by using the dry restitution coefficient $e_{dry} = u_{rebound}/u_{imp}$ such that

$$St_{imp} = \frac{30\varepsilon}{e_{dry}(\log \varepsilon - \log \varepsilon_{max})} = \frac{u_{imp} d_p \rho_p}{9 \rho_f \nu_f}. \tag{4.24}$$

To understand the effect of different ε on St_{thresh}, figure 17(*b*) shows the normalized effective collision frequency as a function of Re_p for different ε. In general, as ε increases, the effective collision frequency decreases and the maximum effective collision frequency shifts to higher Re_p. However, for the range of ε tested, the maximum effective collision frequency occurs when $Re_p = 40$, indicating that the maximum effective collision frequency is not very sensitive to ε. Furthermore, the maximum effective collision frequency coincides with the minimum anisotropy observed in figures 11 and 12, indicating a point in which momentum transfer from the axial to transverse directions is optimal.

5. Summary and conclusions

We studied the effects of the particle Reynolds number on the behaviour of monodispersed spherical particles in PRS simulations of a three-dimensional, liquid–solid fluidized bed.

https://doi.org/10.1017/jfm.2021.780 Published online by Cambridge University Press

The particle Reynolds number was varied by varying the flow rate suspending particles in the axial (z) direction. Analysis of various statistics provided insights into the observed particle motions. Boundary effects associated with the fluidized bed are identified and excluded in statistical calculations to improve accuracy. The wave modes are studied in both physical and spectral spaces to shed light on the source of the particle velocity fluctuations. By separating volume fraction fluctuations into low and high wavenumber components, wave-like behaviour is clearly observed. For low particle Reynolds number ($Re_p = 20$), waves with both low and high wavenumbers are strongly dependent on vertical position and weakly dependent on time. As particle Reynolds number increases, waves with low wavenumber depend strongly both on vertical positions and time while wave motions with high wavenumber are less apparent. Volume fraction fluctuations in spectral space further reveal that high-frequency wave modes are more significant at low particle Reynolds number. Low wavenumber modes can be estimated well with the kinematic wave relationship using linear regression while no discernible kinematic relationship can be observed for high wavenumber modes, indicating that the high wavenumber fluctuations are probably random. Analysis of the root mean square particle velocity fluctuations indicates a maximum at an intermediate particle Reynolds number ($Re_p = 40$) in both the transverse and axial directions.

The decorrelation time scales in the axial and transverse directions reveal that momentum transfer from the axial to the transverse directions is most efficient at $Re_p = 40$ and least efficient at $Re_p = 50$. A sharp decrease in the efficiency of the momentum transfer is observed as Re_p increases from 40 to 50, revealing a transition in the flow regime. Because the length scale over which particle motions decorrelate was less than $1d_p$ for all particle Reynolds numbers simulated, the transition is dominated by porosity effects. By analysing the pairwise distribution function, we found that the probability that particle pairs are aligned at a distance of $2d_p$ decreases with increasing particle Reynolds number. The rate of this decrease revealed two distinct regimes that are consistent with the momentum transfer regimes discussed above.

To understand the mechanisms controlling the flow regimes and the sharp decrease in momentum transfer from the axial to transverse directions, we computed average collision and hydrodynamic stresses as a function of Re_p. The results indicate that the relative magnitude of collision to hydrodynamic effects controls the efficiency of inducing particle velocity fluctuations, momentum transfer and particle alignment. For $20 < Re_p \leq 40$, collisions dominate over hydrodynamic effects but the relative importance of hydrodynamic effects increases, indicating a coexistence of mechanisms related to flow and collisions (regime 1) that leads to the peak in particle velocity fluctuations and momentum transfer. As the particle Reynolds number increases ($Re_p > 40$), hydrodynamic effects dominate over collision effects (regime 2). Due to a lack of effective collisions, particle velocity fluctuations decrease and a sharp decrease in momentum transfer efficiency is observed. The lack of collisions arises from a decrease in the collision frequency with increasing Re_p. We found that it was important to quantify the collision frequency by an effective collision frequency based on collisions satisfying a threshold Stokes number. Defined this way, the effective collision frequency peaks at an Re_p that coincides with that of the highest particle fluctuations and a sharp decrease in momentum transfer.

Our results imply biofilm detachment models in fluidized-bed reactors should focus on collision effects for $Re_p \leq Re_{p,\alpha}$, collision and hydrodynamic effects for $Re_{p,\alpha} < Re_p < Re_{p,\beta}$ and hydrodynamic effects for $Re_p \geq Re_{p,\beta}$, where $Re_{p,\alpha} \approx 40$ and $Re_{p,\beta} \approx 50$ for an Archimedes number of 23 600. This study excludes the effect of adhesive force on biofilm

https://doi.org/10.1017/jfm.2021.780 Published online by Cambridge University Press

and Archimedes number. Further work is required to quantify the effect of adhesive force on particle dynamics and establish a relationship between the optimum particle Reynolds number and Archimedes number. Furthermore, our results imply that mixing within liquid–solid fluidized bed reactors is likely to be optimized at an intermediate Re_p at which particle velocity fluctuations are expected to be the strongest. Indeed, previous fluidized bed reactor studies with a large Archimedes number show that treatment performance is optimized at a similar intermediate $Re_p \approx 30$–40 (Jaafari *et al.* 2014). We anticipate that the results of this study will inform fluidized-bed reactor design and modelling for domestic and industrial wastewater treatment, enabling more reliable and energy-efficient operation.

Acknowledgements. This work used the Extreme Science and Engineering Discovery Environment (XSEDE), which is supported by National Science Foundation grant number ACI-1548562. Simulations were conducted with supercomputer resources under XSEDE Project CTS190063. The authors acknowledge the Texas Advanced Computing Center (TACC) at The University of Texas at Austin for providing HPC resources that have contributed to the research results reported within this paper. We thank H. Lee and S. Balachandar from the University of Florida for providing us with their IBM code. We also thank E. Biegert, B. Vowinckel, T. Köllner and E. Meiburg from the University of California, Santa Babara, for assistance with implementation of the collision models.

Funding. This work was funded by the California Energy Commission (CEC) under CEC project number EPC-16-017, the US NSF Engineering Center for Reinventing of the Nation's Urban Water Infrastructure (ReNUWIt) under award no. 1028968 and Office of Naval Research grant N00014-16-1-2256. This document was prepared as a result of work sponsored in part by the California Energy Commission. It does not necessarily represent the views of the Energy Commission, its employees, or the State of California. Neither the Commission, the State of California, nor the Commission's employees, contractors or subcontractors makes any warranty, express or implied, or assumes any legal liability for the information in this document; nor does any party represent that the use of this information will not infringe upon privately owned rights. This document has not been approved or disapproved by the Commission, nor has the Commission passed upon the accuracy of the information in this document.

Declaration of interests. The authors report no conflict of interest.

Author ORCIDs.
Yinuo Yao https://orcid.org/0000-0001-8328-6072;
Craig S. Criddle https://orcid.org/0000-0002-2750-8547;
Oliver B. Fringer https://orcid.org/0000-0003-3176-6925.

Appendix A. Instantaneous Eulerian volume fraction

In our simulations, the instantaneous Eulerian volume fraction $\phi(\boldsymbol{x}, t)$ can be estimated using a second-order level-set approximation (Kempe & Fröhlich 2012*a*). Defining the particle centre as $\boldsymbol{x}_p$ and Eulerian grid as $\boldsymbol{x}_{ijk}$ where i, j and k represent each direction. The volume fraction of each grid cell is defined as

$$\phi(x_i, y_j, z_k) = \frac{\sum_{l=1}^{8} -\psi_m \mathcal{H}(-\psi_m)}{\sum_{l=1}^{8} |\psi_m|}, \tag{A1}$$

where l is an integer representing the corner of an Eulerian grid, ψ is the level-set function for spheres that is defined as

$$\psi(\boldsymbol{x}, \boldsymbol{x}_p, r_p) = \frac{\|\boldsymbol{x} - \boldsymbol{x}_p\|_2}{r_p} - 1 \tag{A2}$$

https://doi.org/10.1017/jfm.2021.780 Published online by Cambridge University Press

and $\mathcal{H}(-\psi_m)$ is the Heaviside function

$$\mathcal{H}(\alpha) = \begin{cases} 0, & \alpha \leq 0, \\ 1, & \alpha > 0. \end{cases} \tag{A3}$$

To ensure the accuracy of level-approximation for $\phi(\boldsymbol{x}, t)$, we use a grid spacing equivalent to the simulations where $h = d_p/25.6$.

Appendix B. Determination of particle-related stresses

The governing equation of particle motion can be described as

$$m_p \frac{\mathrm{d}\boldsymbol{u}_p}{\mathrm{d}t} = \boldsymbol{F}_{h,p} + \boldsymbol{F}_{col,p} + \boldsymbol{F}_{lub,p} - V_p(\rho_p - \rho_f)\boldsymbol{g}, \tag{B1}$$

where $\boldsymbol{u}_p$ is the translational velocity of a particle, $\boldsymbol{F}_{h,p}$ is the drag force on the particle, $\boldsymbol{F}_{col,p}$ and $\boldsymbol{F}_{lub,p}$ are, respectively, the collision and normal lubrication force on particle p. Fluidization occurs when the weight of particle is balanced by the average drag force. Therefore, the drag force $F_{h,p}$ can be decomposed into two components such that

$$\boldsymbol{F}_{h,p} = \overline{\boldsymbol{F}_{h,p}} + \boldsymbol{F}'_{h,p} = V_p(\rho_p - \rho_f)\boldsymbol{g} + \boldsymbol{F}'_{h,p}, \tag{B2}$$

where $\overline{\boldsymbol{F}_{h,p}}$ is the drag force that balances the weight of particle and $\boldsymbol{F}'_{h,p}$ is the fluctuation force that results in acceleration. By substituting (B2) into (B1), the governing equation can be simplified as

$$m_p \frac{\mathrm{d}\boldsymbol{u}_p}{\mathrm{d}t} = \boldsymbol{F}'_{h,p} + \boldsymbol{F}_{col,p} + \boldsymbol{F}_{lub,p}. \tag{B3}$$

In this study, the stresses due to $\boldsymbol{F}'_{h,p}$, $\boldsymbol{F}_{lub,p}$ and $\boldsymbol{F}_{col,p}$ are defined as hydrodynamic, lubrication and collision stresses, respectively. Since lubrication stress arises when two or more particles move closer to one another due to particle–particle interaction, therefore, lubrication stress is considered separately from the hydrodynamic stress in which the particle motion is only affected by the interaction between fluid and the particle.

The normal lubrication force and collision forces are only non-zero when the separation distance ζ_n between particle centres is less than $d_p + 2h$ and d_p, respectively. As such, the governing equation of particle motion can be rewritten as

$$m_p \frac{\mathrm{d}\boldsymbol{u}_p}{\mathrm{d}t} = \begin{cases} \boldsymbol{F}'_{h,p}, & \text{for } \|\boldsymbol{x}_p - \boldsymbol{x}_q\|_2 > d_p + 2h, \\ \boldsymbol{F}'_{h,p} + \boldsymbol{F}_{lub,p}, & \text{for } d_p < \|\boldsymbol{x}_p - \boldsymbol{x}_q\|_2 \leq d_p + 2h, \\ \boldsymbol{F}_{col,p}, & \text{for } \|\boldsymbol{x}_p - \boldsymbol{x}_q\|_2 \leq d_p, \end{cases} \tag{B4}$$

where x_p and x_q are the particle centre positions.

To determine the stresses as a function of vertical position in the domain, we first discretize the domain into slices with a vertical spacing of $d_p/2$. If we assume the

https://doi.org/10.1017/jfm.2021.780 Published online by Cambridge University Press

Re_p	20	30	40	50	60	70
$\langle\overline{\varepsilon_f}\rangle_x \times 10^2$	0.06 ± 2.17	0.14 ± 1.88	0.16 ± 1.76	0.21 ± 2.80	0.27 ± 1.97	0.26 ± 2.01
$\langle\overline{\varepsilon_f}\rangle_y \times 10^2$	0.06 ± 2.14	0.12 ± 1.91	0.17 ± 1.76	0.21 ± 2.83	0.26 ± 1.93	0.25 ± 1.93
$\langle\overline{\varepsilon_f}\rangle_z \times 10^2$	0.05 ± 2.17	0.12 ± 1.95	0.17 ± 1.78	0.24 ± 2.95	0.28 ± 2.02	0.26 ± 2.07

Table 1. Error $\boldsymbol{\varepsilon}_f$ associated with force balance in (B4).

acceleration of a particle at time step $n + 1/2$ is given by

$$\boldsymbol{a}_p^{n+1/2} = \frac{\boldsymbol{u}_p^{n+1} - \boldsymbol{u}_p^n}{\Delta t}, \tag{B5}$$

then the total force $\boldsymbol{F}_{t,p}$ at time step $n + 1/2$ is $m_p \boldsymbol{a}_p^{n+1/2}$. To demonstrate the validity of (B4), we define an average error metric

$$\langle \boldsymbol{\varepsilon}_f \rangle = \frac{1}{N_p} \sum_{i=1}^{N_p} \frac{m_p \boldsymbol{a}_i^{n+1/2}}{\boldsymbol{F}_{i,rhs}^n} - 1, \tag{B6}$$

where $\boldsymbol{F}_{i,rhs}^n$ is the summation of all forces experienced by the particle i at time n. As shown in table 1, the mean error associated with the approximation is less than 1 % for all cases, demonstrating the validity of (B4).

The hydrodynamic force at time step $n + 1/2$ can be determined as

$$\boldsymbol{F}'_{h,p} = \begin{cases} \boldsymbol{F}_{t,p}, & \text{for } \|\boldsymbol{x}_p - \boldsymbol{x}_q\|_2 > d_p + 2h, \\ \boldsymbol{F}_{t,p} - \boldsymbol{F}_{lub,p}, & \text{for } d_p < \|\boldsymbol{x}_p - \boldsymbol{x}_q\|_2 \le d_p + 2h, \end{cases} \tag{B7}$$

and the hydrodynamic stress over particle surface area $(\sigma_{hydro,p})^{n+1/2} = \boldsymbol{F}'_{h,p}/(\pi d_p^2)$ can be calculated. The hydrodynamic stress for a particle bin k can be calculated as

$$(\boldsymbol{\sigma}_{hydro})_k = \frac{1}{N} \sum_{n=1}^{N_p} \sum_{t=1}^{N_t} \frac{(|\boldsymbol{F}'_h|)_i^t}{\pi d_p^2} \mathbf{1}_{z_l < z_i < z_u}(z_i), \tag{B8}$$

where $N = \sum^{N_t N_p} \mathbf{1}_{z_l < z_i < z_u}(z_i)$ is the number of samples in each bin, z_i is the vertical position of particle i, $\boldsymbol{e}$ is vector of ones and $\mathbf{1}_{z_l < z_i < z_u}(z_i)$ is the indicator function that is defined as

$$\mathbf{1}_{z_l < z_p < z_u}(z_i) = \begin{cases} 1, & z_l < z_p < z_u, \\ 0, & \text{otherwise.} \end{cases} \tag{B9}$$

In the simulations, the collision model is based on the adaptive collision time model (known as ACTM) proposed by Kempe & Fröhlich (2012*a*) and tangential collision models by Biegert *et al.* (2017). In the adaptive collision time model, each collision is assumed to occur over $10\Delta t$ instead of Δt in the soft-sphere collision model. At each time step, the normal contact force $\boldsymbol{F}_{col}$ is determined and the contributions of all collisions at a bin k is determined with

$$(\boldsymbol{\sigma}_{col})_k = \frac{1}{N} \sum_{n=1}^{N_p} \sum_{t=1}^{N_t} \frac{(|\boldsymbol{F}_{con}|)_i^t}{\pi d_p^2} \mathbf{1}_{z_l < z_i < z_u}(z_i). \tag{B10}$$

A similar procedure can be applied to the lubrication stress after assuming the lubrication forces are also stretched over several time steps. The contributions of all

https://doi.org/10.1017/jfm.2021.780 Published online by Cambridge University Press

lubrication forces in a bin k is determined with

$$(\boldsymbol{\sigma}_{lub})_k = \frac{1}{N}\sum_{n=1}^{N_p}\sum_{t=1}^{N_t}\frac{(|\boldsymbol{F}_{lub}|)_i^t}{\pi d_p^2}\mathbf{1}_{z_l<z_i<z_u}(z_i). \tag{B11}$$

References

Akiki, G., Jackson, T.L. & Balachandar, S. 2016 Force variation within arrays of monodisperse spherical particles. *Phys. Rev. Fluids* **1** (4), 044202.

Akiki, G., Jackson, T.L. & Balachandar, S. 2017*a* Pairwise interaction extended point-particle model for a random array of monodisperse spheres. *J. Fluid Mech.* **813**, 882–928.

Akiki, G., Moore, W.C. & Balachandar, S. 2017*b* Pairwise-interaction extended point-particle model for particle-laden flows. *J. Comput. Phys.* **351**, 329–357.

Bagchi, P. & Balachandar, S. 2003 Effect of turbulence on the drag and lift of a particle. *Phys. Fluids* **15** (11), 3496–3513.

Biegert, E.K. 2018 Eroding uncertainty: towards understanding flows interacting with mobile sediment beds using grain-resolving simulations. PhD thesis, UC Santa Barbara.

Biegert, E., Vowinckel, B. & Meiburg, E. 2017 A collision model for grain-resolving simulations of flows over dense, mobile, polydisperse granular sediment beds. *J. Comput. Phys.* **340**, 105–127.

Chang, H.T., Rittmann, B.E., Amar, D., Heim, R., Ehlinger, O. & Lesty, Y. 1991 Biofilm detachment mechanisms in a liquid-fluidized bed. *Biotechnol. Bioengng* **38** (5), 499–506.

Chow, E., Cleary, A.J. & Falgout, R.D. 1998 Design of the HYPRE preconditioner library. In *SIAM Workshop on Object Oriented Methods for Inter-operable Scientific and Engineering Computing*. SIAM.

Costa, P., Boersma, B.J., Westerweel, J. & Breugem, W.-P. 2015 Collision model for fully resolved simulations of flows laden with finite-size particles. *Phys. Rev.* E **92** (5), 053012.

Derksen, J.J. & Sundaresan, S. 2007 Direct numerical simulations of dense suspensions: wave instabilities in liquid-fluidized beds. *J. Fluid Mech.* **587**, 303–336.

Di Felice, R. 1995 Hydrodynamics of liquid fluidisation. *Chem. Engng Sci.* **50** (8), 1213–1245.

Di Felice, R. 1999 The sedimentation velocity of dilute suspensions of nearly monosized spheres. *Intl J. Multiphase Flow* **25** (4), 559–574.

Di Felice, R. & Parodi, E. 1996 Wall effects on the sedimentation velocity of suspensions in viscous flow. *AIChE J.* **42** (4), 927–931.

Dieterich, J.H. 1972 Time-dependent friction in rocks. *J. Geophys. Res.* **77** (20), 3690–3697.

Duru, P., Nicolas, M., Hinch, J. & Guazzelli, É. 2002 Constitutive laws in liquid-fluidized beds. *J. Fluid Mech.* **452**, 371–404.

Esteghamatian, A., Hammouti, A., Lance, M. & Wachs, A. 2017 Particle resolved simulations of liquid/solid and gas/solid fluidized beds. *Phys. Fluids* **29** (3), 033302.

Falgout, R.D. 2006 An introduction to algebraic multigrid. *Comput. Sci. Engng* **8** (6), 24–33.

Finn, J. & Apte, S.V. 2013 Relative performance of body fitted and fictitious domain simulations of flow through fixed packed beds of spheres. *Intl J. Multiphase Flow* **56**, 54–71.

Foerster, S.F., Louge, M.Y., Chang, H. & Allia, K. 1994 Measurements of the collision properties of small spheres. *Phys. Fluids* **6** (3), 1108–1115.

Garside, J. & Al-Dibouni, M.R. 1977 Velocity-voidage relationships for fluidization and sedimentation in solid–liquid systems. *Ind. Engng Chem. Process Des. Dev.* **16** (2), 206–214.

Geldart, D. 1973 Types of gas fluidization. *Powder Technol.* **7** (5), 285–292.

Gjaltema, A., Vinke, J.L., van Loosdrecht, M.C. & Heijnen, J.J. 1997 Abrasion of suspended biofilm pellets in airlift reactors: importance of shape, structure, and particle concentrations. *Biotechnol. Bioengng* **53** (1), 88–99.

Ham, J.M. & Homsy, G.M. 1988 Hindered settling and hydrodynamic dispersion in quiescent sedimenting suspensions. *Intl J. Multiphase Flow* **14** (5), 533–546.

Hamid, A., Molina, J.J. & Yamamoto, R. 2014 Direct numerical simulations of sedimenting spherical particles at non-zero Reynolds number. *RSC Adv.* **4** (96), 53681–53693.

Jaafari, J., Mesdaghinia, A., Nabizadeh, R., Hoseini, M., Kamani, H. & Mahvi, A.H. 2014 Influence of upflow velocity on performance and biofilm characteristics of Anaerobic Fluidized Bed Reactor (AFBR) in treating high-strength wastewater. *J. Environ. Health Sci. Engng* **12** (1), 139.

Joseph, G.G. & Hunt, M.L. 2004 Oblique particle–wall collisions in a liquid. *J. Fluid Mech.* **510**, 71–93.

Joseph, G.G., Zenit, R., Hunt, M.L. & Rosenwinkel, A.M. 2001 Particle–wall collisions in a viscous fluid. *J. Fluid Mech.* **433**, 329–346.

https://doi.org/10.1017/jfm.2021.780 Published online by Cambridge University Press

KEMPE, T. & FRÖHLICH, J. 2012*a* An improved immersed boundary method with direct forcing for the simulation of particle laden flows. *J. Comput. Phys.* **231** (9), 3663–3684.

KEMPE, T. & FRÖHLICH, J. 2012*b* Collision modelling for the interface-resolved simulation of spherical particles in viscous fluids. *J. Fluid Mech.* **709**, 445–489.

KIDANEMARIAM, A.G., CHAN-BRAUN, C., DOYCHEV, T. & UHLMANN, M. 2013 Direct numerical simulation of horizontal open channel flow with finite-size, heavy particles at low solid volume fraction. *New J. Phys.* **15** (2), 025031.

KRIEBITZSCH, S.H.L., VAN DER HOEF, M.A. & KUIPERS, J.A.M. 2013 Fully resolved simulation of a gas-fluidized bed: A critical test of DEM models. *Chem. Engng Sci.* **91**, 1–4.

LEE, H. & BALACHANDAR, S. 2010 Drag and lift forces on a spherical particle moving on a wall in a shear flow at finite Re. *J. Fluid Mech.* **657**, 89–125.

LEE, H., HA, M.Y. & BALACHANDAR, S. 2011 Rolling/sliding of a particle on a flat wall in a linear shear flow at finite Re. *Intl J. Multiphase Flow* **37** (2), 108–124.

LEGENDRE, D., ZENIT, R., DANIEL, C. & GUIRAUD, P. 2006 A note on the modelling of the bouncing of spherical drops or solid spheres on a wall in viscous fluid. *Chem. Engng Sci.* **61** (11), 3543–3549.

LU, J., PETERS, E.A.J.F. & KUIPERS, J.A.M. 2020 Direct numerical simulation of mass transfer in bidisperse arrays of spheres. *AIChE J.* **66** (1), 1–17.

NICOLAI, H., HERZHAFT, B., HINCH, E.J., OGER, L. & GUAZZELLI, E. 1995 Particle velocity fluctuations and hydrodynamic self-diffusion of sedimenting non-Brownian spheres. *Phys. Fluids* **7** (1), 12–23.

NICOLELLA, C., CHIARLE, S., DI FELICE, R. & ROVATTI, M. 1997 Mechanisms of biofilm detachment in fluidized bed reactors. *Water Sci. Technol.* **36** (1), 229–235.

NICOLELLA, C., DI FELICE, R. & ROVATTI, M. 1996 An experimental model of biofilm detachment in liquid fluidized bed biological reactors. *Biotechnol. Bioengng* **51** (6), 713–719.

OZEL, A., BRÄNDLE DE MOTTA, J.C., ABBAS, M., FEDE, P., MASBERNAT, O., VINCENT, S., ESTIVALEZES, J.-L. & SIMONIN, O. 2017 Particle resolved direct numerical simulation of a liquid–solid fluidized bed: comparison with experimental data. *Intl J. Multiphase Flow* **89**, 228–240.

PAN, H., CHEN, X.-Z., LIANG, X.-F., ZHU, L.-T. & LUO, Z.-H. 2016 CFD simulations of gas–liquid–solid flow in fluidized bed reactors – a review. *Powder Technol.* **299**, 235–258.

PESKIN, C.S. 1977 Numerical analysis of blood flow in the heart. *J. Comput. Phys.* **25** (3), 220–252.

RAI, M. & MOIN, P. 1991 Direct simulations of turbulent flow using finite-difference schemes. *J. Comput. Phys.* **96** (1), 15–53.

RICHARDSON, J.F. & ZAKI, W.N. 1954 Sedimentation and fluidisation: part I. *Trans. Inst. Chem. Engng* **32**, 35–53.

RITTMANN, B.E. & MCCARTY, P.L. 2018 *Environmental Biotechnology: Principles and Applications*. McGraw-Hill Education.

ROMA, A.M., PESKIN, C.S. & BERGER, M.J. 1999 An adaptive version of the immersed boundary method. *J. Comput. Phys.* **153** (2), 509–534.

SHAJAHAN, T. & BREUGEM, W.-P. 2020 Influence of concentration on sedimentation of a dense suspension in a viscous fluid. *Flow Turbul. Combust.* **105** (2), 537–554.

SHIN, C., BAE, J. & MCCARTY, P.L. 2012 Lower operational limits to volatile fatty acid degradation with dilute wastewaters in an anaerobic fluidized bed reactor. *Bioresour. Technol.* **109**, 13–20.

SHIN, C., LEE, E., MCCARTY, P.L. & BAE, J. 2011 Effects of influent DO/COD ratio on the performance of an anaerobic fluidized bed reactor fed low-strength synthetic wastewater. *Bioresour. Technol.* **102** (21), 9860–9865.

SHIN, C., MCCARTY, P.L., KIM, J. & BAE, J. 2014 Pilot-scale temperate-climate treatment of domestic wastewater with a staged anaerobic fluidized membrane bioreactor (SAF-MBR). *Bioresour. Technol.* **159**, 95–103.

SUNDARESAN, S. 2003 Instabilities in fluidized beds. *Annu. Rev. Fluid Mech.* **35** (1), 63–88.

TANG, Y., PETERS, E.A.J.F., KUIPERS, J.A.M., KRIEBITZSCH, S.H.L. & VAN DER HOEF, M.A. 2015 A new drag correlation from fully resolved simulations of flow past monodisperse static arrays of spheres. *AIChE J.* **61** (2), 688–698.

TENNETI, S., GARG, R. & SUBRAMANIAM, S. 2011 Drag law for monodisperse gas–solid systems using particle-resolved direct numerical simulation of flow past fixed assemblies of spheres. *Intl J. Multiphase Flow* **37** (9), 1072–1092.

UHLMANN, M. 2005 An immersed boundary method with direct forcing for the simulation of particulate flows. *J. Comput. Phys.* **209** (2), 448–476.

UHLMANN, M. & DOYCHEV, T. 2014 Sedimentation of a dilute suspension of rigid spheres at intermediate Galileo numbers: the effect of clustering upon the particle motion. *J. Fluid Mech.* **752**, 310–348.

https://doi.org/10.1017/jfm.2021.780 Published online by Cambridge University Press

VERMA, V., PADDING, J.T., DEEN, N.G. & HANS KUIPERS, J.A.M. 2015 Effect of bed size on hydrodynamics in 3-D gas-solid fluidized beds. *AIChE J.* **61** (5), 1492–1506.

VERMA, V., PADDING, J.T., DEEN, N.G. & KUIPERS, J.A.M.H. 2014 Numerical investigation on the effect of pressure on fluidization in a 3D fluidized bed. *Ind. Engng Chem. Res.* **53** (44), 17487–17498.

WALLIS, G.B. 2020 *One-Dimensional Two-Phase Flow*. Courier Dover Publications.

WANG, Z., FAN, J. & LUO, K. 2008 Combined multi-direct forcing and immersed boundary method for simulating flows with moving particles. *Intl J. Multiphase Flow* **34** (3), 283–302.

WILLEN, D.P. & PROSPERETTI, A. 2019 Resolved simulations of sedimenting suspensions of spheres. *Phys. Rev. Fluids* **4** (1), 014304.

WILLEN, D.P., SIERAKOWSKI, A.J., ZHOU, G. & PROSPERETTI, A. 2017 Continuity waves in resolved-particle simulations of fluidized beds. *Phys. Rev. Fluids* **2** (11), 114305.

YANG, M., YU, D., LIU, M., ZHENG, L., ZHENG, X., WEI, Y., WANG, F. & FAN, Y. 2017 Optimization of MBR hydrodynamics for cake layer fouling control through CFD simulation and RSM design. *Bioresour. Technol.* **227**, 102–111.

YAO, Y., CRIDDLE, C.S. & FRINGER, O.B. 2021*a* Comparison of the properties of segregated layers in a bidispersed fluidized bed to those of a monodispersed fluidized bed. *Phys. Rev. Fluids* **6**, 084306.

YAO, Y., CRIDDLE, C.S. & FRINGER, O.B. 2021*b* The effects of particle clustering on hindered settling in high-concentration particle suspensions. *J. Fluid Mech.* **920**, A40.

YIN, X. & KOCH, D.L. 2007 Hindered settling velocity and microstructure in suspensions of solid spheres with moderate Reynolds numbers. *Phys. Fluids* **19** (9), 093302.

YIN, X. & KOCH, D.L. 2008 Lattice-Boltzmann simulation of finite Reynolds number buoyancy-driven bubbly flows in periodic and wall-bounded domains. *Phys. Fluids* **20** (10), 103304.

YU, A. & XU, B. 2003 Particle-scale modelling of gas-solid flow in fluidisation. *J. Chem. Technol. Biotechnol.* **78** (2–3), 111–121.

ZAIDI, A.A., TSUJI, T. & TANAKA, T. 2015 Hindered settling velocity & structure formation during particle settling by direct numerical simulation. *Procedia Engng* **102**, 1656–1666.

ZANG, Y., STREET, R.L. & KOSEFF, J.R. 1994 A non-staggered grid, fractional step method for time-dependent incompressible Navier–Stokes equations in curvilinear coordinates. *J. Comput. Phys.* **114** (1), 18–33.

ZENIT, R. & HUNT, M.L. 2000 Solid fraction fluctuations in solid–liquid flows. *Intl J. Multiphase Flow* **26** (5), 763–781.

ZENIT, R., HUNT, M.L. & BRENNEN, C.E. 1997 Collisional particle pressure measurements in solid–liquid flows. *J. Fluid Mech.* **353**, 261–283.

ZHANG, Z. & PROSPERETTI, A. 2005 A second-order method for three-dimensional particle simulation. *J. Comput. Phys.* **210** (1), 292–324.

https://doi.org/10.1017/jfm.2021.780 Published online by Cambridge University Press